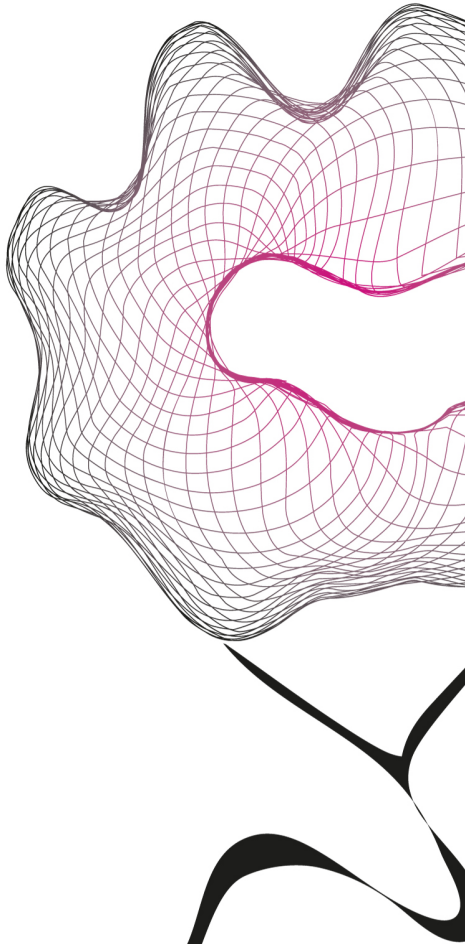


MASTER THESIS



# SCAFFOLD- FREE HEART TISSUE ASSEMBLY: ORCHESTRATING CELLS INTO FUNCTIONAL STRUCTURES

Danique Helena Nakken

FACULTY OF ENGINEERING TECHNOLOGY  
DEPARTMENT OF BIOMECHANICAL ENGINEERING

**EXAMINATION COMMITTEE**

Dr. Ir. Jeroen Rouwkema  
Dr. Vasileios Trikalitis  
Dr. Verena Schwach  
Jun.-Prof. Dr.-Ing. Daniela Duarte Campos  
Dr. Oscar O'Dwyer

DOCUMENT NUMBER

-



UNIVERSITÄT  
HEIDELBERG  
ZUKUNFT  
SEIT 1386

UNIVERSITY OF TWENTE.

# Master Thesis

---

## Scaffold-free Heart Tissue Assembly: Orchestrating Cells into Functional Structures

by Danique Helena Nakken

*at*

University of Twente

*and*

Ruprecht-Karls-Universität Heidelberg

Zentrum für Molekulare Biologie der Universität Heidelberg

Bioprinting & Tissue Engineering – Duarte Campos Bioprinting Lab

LIGHTHEART: Surgical optogenetic bioprinting of engineered cardiac muscle

Supervision:

Dr.-Ing. Jeroen Rouwkema

Dr. Verena Schwach

Dr. Vasileios Trikalitis

Jun.-Prof. Dr.-Ing. Daniela Duarte Campos

Dr. Oscar O'Dwyer Lancaster-Jones



09.12.2024

DC bioprintinglab

## Abstract (ENG)

Cardiovascular disease is the leading cause of death worldwide, with myocardial infarction (MI) responsible for approximately 1 in 6 fatalities. [1] Tissue engineering and regenerative medicine aim to address this issue by repairing, maintaining, or enhancing the function of damaged tissues. Implantable therapeutics such as cell-based therapies are known to be a promising treatment method. However, creating fully functional, mature, and non-immunogenic tissues *in vitro* remains a challenge. For cardiac tissue, the functionality heavily depends on cell alignment, which is crucial for promoting electrical signal propagation and force generation. [2], [3]

This study aimed to develop a system to control cardiac tissue self-assembly using spheroids as building blocks. Microfeature moulds were fabricated to guide spheroid fusion and promote cell alignment within larger 3D *in vitro* tissues. A stereolithography (SLA) printer was used to fabricate a positive resin mould in order to cast negative agarose moulds with a seeding area of 10 mm<sup>2</sup>. The print resolution was improved by exploring exposure time (1s) and print angle (0°), and sequentially agarose was casted, establishing a protocol using centrifugation (700 rpm for 15s).

Human dermal fibroblast (HDF) spheroids with a diameter of 160 µm were used for prototyping to optimize the mould design and spheroid seeding density to 1000 spheroids. This resulted in successful spheroid fusion and tissue formation within the microfeatures with a tissue thickness ranging from 65 µm to 117 µm. Tissue area reduction analysis using ImageJ and histology showed a relationship of structural barriers and spheroid coherence. Furthermore, cell alignment was determined staining the actin of mixed rat cardiomyocyte-HDF spheroids, indicating a relationship of structural barriers and cellular organization. This provides insights into strategies for the production of functional heart tissue using spheroids as building blocks.

## Abstract (NL)

Hart- en vaatziekten zijn wereldwijd de meest voorkomende doodsoorzaak, waarbij myocardinfarcten (MI) verantwoordelijk zijn voor ongeveer 1 op de 6 sterfgevallen. [1] Weefselengineering en regeneratieve geneeskunde zijn erop gericht dit probleem aan te pakken door beschadigde weefsels te repareren, te onderhouden of de functie ervan te verbeteren. Implanteerbare therapeutica zoals celtherapieën staan bekend als een veelbelovende behandelmethode. Het blijft echter een uitdaging om volledig functioneel, volgroeid en niet-immunogeen weefsel *in vitro* te creëren. Voor hartweefsel hangt de functionaliteit sterk af van de uitlijning van de cellen, die cruciaal is voor het bevorderen van de verspreiding van elektrische signalen en het genereren van kracht. [2], [3]

Deze studie was gericht op de ontwikkeling van een systeem om de zelfassemblage van hartweefsel te controleren met behulp van sferoiden als bouwstenen. Er werden microvormen gemaakt om de fusie van sferoiden te geleiden en de uitlijning van cellen binnen grotere 3D *in vitro* weefsels te bevorderen. Een stereolithografieprinter (SLA) werd gebruikt om een positieve harsmal te maken om negatieve agarose mallen met een zaaigebied van 10 mm<sup>2</sup> te gieten. De printresolutie werd verbeterd door de belichtingstijd (1s) en printhoek (0°) te verkennen en vervolgens werd een agarose gietprotocol opgesteld met centrifugeren (700 rpm gedurende 15s).

Humane dermale fibroblasten (HDF) sferoiden met een diameter van 160 µm werden gebruikt voor prototyping om het ontwerp en de dichtheid voor het zaaien van sferoiden te optimaliseren tot 1000 sferoiden. Dit resulteerde in een succesvolle fusie van de sferoiden en weefselvorming binnen de microvormen met een weefseldikte variërend van 65 µm tot 117 µm. Analyse van de reductie van het weefseloppervlak met ImageJ en histologie toonde een verband aan tussen structurele barrières en de coherentie van de sferoiden. Bovendien werd de uitlijning van cellen bepaald door actine te kleuren op gemengde ratten cardiomyocyte-HDF-sferoiden, wat duidt op een verband tussen structurele barrières en cellulaire organisatie. Dit biedt inzicht in strategieën voor de productie van functioneel hartweefsel met behulp van sferoiden als bouwstenen.

## Keywords

Cardiac tissue, Spheroids, Self-assembly, 3D printed moulds, Scaffold-free

## Abbreviations

CMs	Cardiomyocytes
CM-HDF 3	Rat cardiomyocytes and human dermal fibroblasts mixed spheroid with a pre-culture time of three days
ECM	Extracellular matrix
ESCs	Embryonic stem cells
HDF	Human dermal fibroblasts
HDF 3	Human dermal fibroblasts spheroid with a pre-culture time of three days
HDF 4	Human dermal fibroblasts spheroid with a pre-culture time of four days
hiPSCs	Human induced pluripotent stem cells
iPSCs	Induced pluripotent stem cells
MI	Myocardial infarction
MTPD®	MicroTissues® 3DPetri Dishes®
NHF	Normal human fibroblasts
PDMS	Polydimethylsiloxane
PFA	Paraformaldehyde
PSCs	Pluripotent stem cell
rpm	Revolutions per minute
SD	Standard deviation
SLA	Stereolithography
wt%	Weight percentage
2D	2 Dimensional
3D	3 Dimensional

# Table of Contents

Introduction .....	- 1 -
1. Background.....	- 1 -
1.1. Tissue engineering and regenerative medicine .....	- 1 -
1.2. The human heart .....	- 1 -
1.3. Cardiovascular disease .....	- 1 -
1.4. Cardiovascular disease treatment strategies and limitations.....	- 1 -
1.5. Improved cardiac tissue functionality in vitro.....	- 2 -
1.6. 3D cell culture: Spheroids .....	- 3 -
1.7. Current cardiac tissue fabrication methodologies.....	- 4 -
1.8. Introducing alignment into engineered cardiac tissues .....	- 5 -
1.9. Mould fabrication .....	- 7 -
1.10. Moulding materials .....	- 7 -
2. Aim and Objective .....	- 8 -
Materials and Methods .....	- 9 -
Results .....	- 13 -
1. Mould fabrication.....	- 13 -
1.1 Cardiac patch mould requirements.....	- 13 -
1.2 Microfeature printability.....	- 14 -
1.3 Mould design .....	- 16 -
1.4 Mould design printability.....	- 17 -
1.5 Agarose casting.....	- 18 -
2. Spheroid compaction .....	- 20 -
3. Spheroid fusion .....	- 21 -
4. Microtissue .....	- 22 -
4.1. Spheroid seeding requirements for homogeneous tissue fusion .....	- 22 -
4.2. Exploring spheroid pre-culture time for tissue fusion .....	- 24 -
4.3. Cardiomyocyte mixed spheroid fusion .....	- 26 -
Discussion .....	- 28 -
Conclusion.....	- 35 -

# Introduction

## 1. Background

### 1.1. Tissue engineering and regenerative medicine

In tissue engineering and regenerative medicine, the aim is to repair, maintain, or enhance the function of tissues to restore injured or disease affected organs. The approach often combines living cells and biomaterials to create implantable therapeutics or 3D *in vitro* models, to gain fundamental cell biology knowledge. [2], [3]

### 1.2. The human heart

The human heart is an organ, that ensures blood supply throughout the whole body. It is composed of three main layers: the endocardium, myocardium, and epicardium. The endocardium is the inner heart wall that is in contact with blood. The outer heart layer is called epicardium, which function is, to protect the heart and support the regeneration of some myocardium cells. The middle layer, the myocardium, is the thickest layer of all three. Around 75% of the heart volume is occupied by the cell type cardiomyocytes (CMs). Other abundant cell types are endothelial cells, pericytes, and fibroblasts. The CMs are the force generating and electrical signal spreading cells, that allow rhythmic contraction in order to pump blood throughout the body. This contraction is a coordinated electromechanical activity and highly relies on an anisotropic cell structure, guiding the directionality of force. [3], [4], [5], [6]

### 1.3. Cardiovascular disease

Cardiovascular disease is the leading cause of death globally, with myocardial infarction (MI) accounting for about 1 in every 6 fatalities. [1] MI, also known as a heart attack, is an occlusion of the coronary artery, causing a lack of blood supply resulting in cell death and myocardium damage. CMs have an insufficient regeneration potential, which limits their ability to recover the heart function. Subsequent damage is caused by the cardiac remodeling process, which lowers the heart function by forming fibroblastic scar tissue and extracellular matrix degradation, which can lead to heart failure. [4]

### 1.4. Cardiovascular disease treatment strategies and limitations

To restore the cardiac function and to counteract heart failure by overcoming long-term myocardium damage, different approaches of implantable therapeutics are explored. One of the current treatments is a heart transplantation. Unfortunately, this technique is limited due to the shortage of donor organs and has the disadvantage of requiring immunosuppressive drugs, including the risk of organ rejection. The growing shortage of donor organs, coupled with the projected rise in cardiovascular disease cases in the coming decades, highlights an urgent need for alternative treatments. Fortunately, cell-based therapies present a promising solution. [3]

The current cell-based approaches to restore damaged myocardium, primarily focus on developing tissues in the millimeter to centimeter range, rather than replacing the entire organ. While engineering tissue may appear less complex than creating a whole organ, producing a fully functional and mature cardiac tissue *in vitro* that is nonimmunogenic, remains a significant challenge. [7], [8], [9]

The following three key limitations are causing the development of such a tissue to be a challenge:

- i. “The applicability of human heart cells in cardiac tissue engineering” [8]
- ii. “Overcoming size limitations” [8]
- iii. “Providing fully biocompatible tissue-engineered muscle” [8]

(i) To fabricate a cardiac tissue, a high number of cells especially CMs are needed. Unfortunately, human primary CMs have significant limitations, as they are difficult to obtain, have a short lifespan, and undergo profound structural and functional remodeling, leading to dedifferentiation and reduced viability. These challenges make them less suitable for long-term studies or tissue engineering applications.

As an alternative, non-human cell lines are commonly used for preliminary testing. Examples include rat embryonic myoblasts (H9c2), mouse cardiomyocytes (HL-1), and primary CMs isolated from chicken embryos or neonatal rats. However, the acquired cell population are not always completely homogeneous as they consist of cardiac cell types like ventricular-type, nodal and atrial-like action potentials. Additionally, although these models are more accessible and easier to work with, their relevance to human physiology is limited.

To overcome these challenges, induced pluripotent stem cells (iPSCs) have become an attractive solution. Pluripotent stem cells (PSCs), which include both embryonic stem cells (ESCs) derived from the blastocyst and iPSCs reprogrammed from somatic cells, have the unique ability to self-renew and differentiate into any cell type in the human body. Human iPSC (hiPSCs)-derived cells are particularly promising, as they can replicate patient-specific physiology while bypassing the ethical concerns associated with ESCs. Additionally, since cell heterogeneity is required to improve tissue function, using hiPSCs can create a more *in vivo*-like environment (see Fig. 1). [6], [7], [10]

(ii) In tissue engineering, upscaling is challenging because, without vascularization, the supply of nutrients and oxygen is limited to a restricted radius, due to diffusion. Nevertheless, to accomplish a meaningful contraction force impact *in vivo*, when implanting a cardiac tissue onto the patient’s heart, physiological muscle diameters of minimal 10 mm are necessary. [8], [11]

(iii) The primary goal of cardiac tissue engineering is to repair, maintain, or enhance the patient’s heart function, which depends heavily on the tissue’s ability to generate force. This requires the cardiac tissue to exhibit contractile activity, either through spontaneous contractions or electrical stimulation. [8]

### 1.5. Improved cardiac tissue functionality *in vitro*

The conventional two-dimensional (2D) cell culture, where cells grow on a flat adherent layer, is a well-established and cost-effective method to expand cell lines. Nevertheless, in a 2D culture, cells are often surrounded by a large volume of extracellular fluid. This fluid dilutes the autocrine and paracrine cell signals, reducing their local impact and *in vivo* like behavior. A three-dimensional (3D) culture, on the other hand is a dense cell structure with defined extracellular space, allowing individual cells to adopt specific shapes and form matrix adhesions. This creates a more *in vivo* like cell environment including local paracrine and autocrine cell effect, enhancing tissue functional, metabolic, and structural maturation (see Fig. 1). This maturation is especially crucial for electrically active tissues like the myocardium. Examples of 3D culture are spheroids (see introduction section 1.6) and organoids but also engineered microarchitectures (see introduction section 1.7 and 1.8) like cardiac patches, rings, bands, and strips.

Interestingly, by incorporating an anisotropic 3D cell alignment structure (see introduction section 1.8) to these microarchitectures, both physiological and pathophysiological functions are improved. Additional strategies to improve cardiac tissue functionality are methods like electrical stimulation, dynamic culture conditions, and co-culture techniques. For instance, co-culturing hiPSC-CMs with fibroblasts provides a structurally supportive environment that promotes tissue remodeling, improves cell–cell communication, and enhances the maturation of hiPSC-CMs. [3], [7], [10], [12]

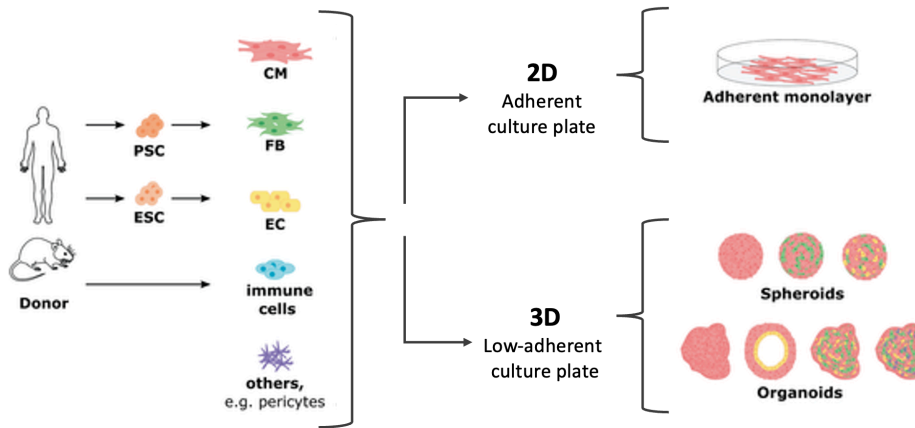


Fig. 1: Cardiac cell source such as human and animal for primary cells but also for pluripotent stem cell (PSC) and embryonic stem cell (ESC) for cell differentiation into cardiomyocytes (CMs), fibroblasts (FB), endothelial cells (EC), immune cells and others like pericytes. Examples of scaffold-free cell culturing methods are 2D: adherent culture plate forming an adherent monolayer and 3D: low adherent culture plates causing the formation of spheroid or organoids depending on the initial cell type. [7]

### 1.6. 3D cell culture: Spheroids

Spheroids are cell aggregates that produce their own extracellular matrix (ECM) and can be composed of a single cell type or multiple cell types. They form through self-assembly when cells are cultured on a substrate, that prevents cell adhesion and promote cell-cell interactions. Therefore, a spheroid is the final structure with minimized surface energy and area. [13]

Key methods for spheroid production include ultra-low attachment plates (surface chemistry), hanging drop technique (gravity), and microfluidic systems (flow-based), but there are also techniques that are based on centrifugal force or acoustic wave [10], [12], [14], [15]

Two main categories of 3D cell culture approaches are scaffold-free and scaffold-based techniques. While both rely on the use of cells, scaffold-based techniques also incorporate biomaterials such as hydrogels, Matrigel®, fibrin, thrombin, and/or collagen, which provide structural support and can be adjusted based on the cell types. Nevertheless, the use of biomaterials can cause challenges like, matrix degradation, insufficient mechanical properties and immunogenicity. [7], [16]

The main limitation of spheroids is their size. When spheroids are composed of too many cells, the spheroid diameter increases, and the core becomes necrotic due to limited oxygen and nutrition supply. This phenomenon occurs when spheroids reach a diameter of several hundred micrometers. [17]

Despite the spheroid size limitation, they remain valuable as building blocks for tissue engineering, with early proof-of-concept models demonstrating successful microvascularization to address the challenge of necrotic core formation. [7] Nevertheless, there are several techniques to assemble spheroids like moulding, acoustic assembly and bioprinting. [18], [19], [20] Choosing the techniques depends on the desired tissue architecture and function. Table 1 lists two papers where cardiac spheroids were used as building blocks. When using spheroids, their fusion behavior can be manipulated by changing the spheroid size, aggregate size, cell type (uni- or multicellular) as well as the pre-culture time. [20], [21], [22], [23]

Table 1: Literature overview of 3D in vitro models using cardiac spheroids as building blocks

Cite	Cell type and biomaterials	Spheroid production method	Spheroid fusion method
[16]	“Rat neonatal ventricular cardiomyocytes, human dermal fibroblasts, and human coronary microartery endothelial cells” [16]	Ultralow attachment plate	Spheroid layer on ultralow attachment plate
[24]	Cardiac and endothelial cells, vascular endothelial growth factor	Pellet centrifugation	Extrusion-based printing to create a donut shape



## 1.7. Current cardiac tissue fabrication methodologies

Some of the recent cardiac tissue fabrication approaches can be seen in Fig. 2. It includes five categories: Decellularized bioscaffolds, electrospinning, bioprinting, microfabrication, and hydrogels. Decellularization is a method used to remove all cells from the tissue structure while preserving the well-defined and composed extracellular matrix (ECM). However, this approach requires access to organs, presenting challenges due to the shortage of human donors. Alternatively, off-the-shelf animal organs can be used, but this raises ethical concerns. Electrospinning uses natural or synthetic materials that get passed through an electrostatic field by gravitational force in order to braid, weave, or knit a fibrous network, mimicking the native ECM. In bioprinting often, a layer-by-layer structure of living cells and biomaterials get deposit onto a printbed or into a supportive material, allowing the print of complex tissue models. Hydrogels, on the other hand, have the ability to either embed cells or to create a mould to guide cell structure. Hydrogels are biocompatible materials with a high-water absorption, enabling efficient diffusion of oxygen and the transport of metabolites. The material is versatile, allowing for modification or functionalization, and can be moulded into various geometries while being scalable. Microfabrication offers the advantage of finely engineering material features to mimic *in vivo* tissue conditions by creating defined topographies that promote anisotropic tissue organization. [6]

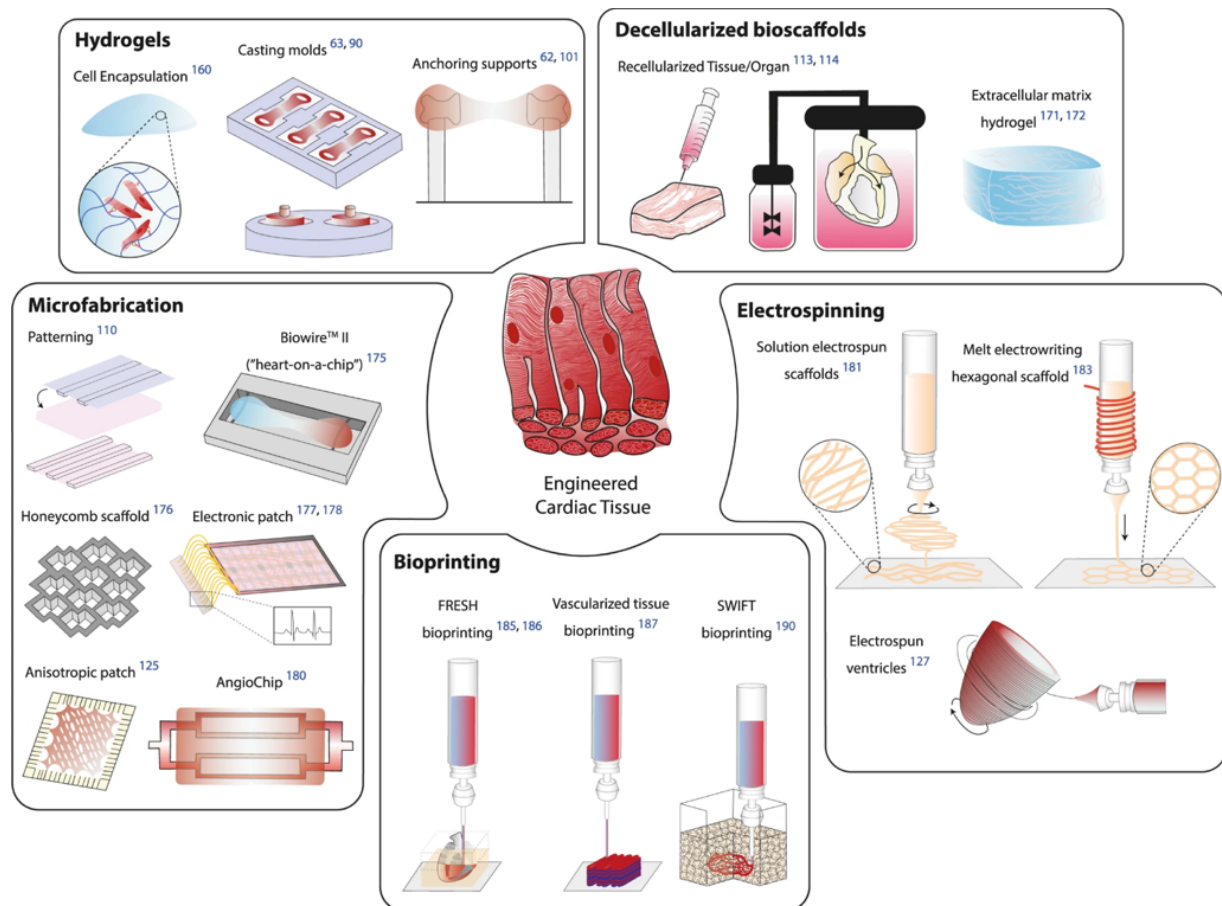


Fig. 2: Current cardiac tissue fabrication approaches like decellularized bioscaffolds including decellularized tissue/ organ and extracellular matrix hydrogel, electrospinning including solution electrospun scaffolds and melt electrowriting elliptical scaffold, bioprinting methods like FRESH (Freeform Reversible Embedding of Suspended Hydrogels), vascularized tissue bioprinting and SWIFT (Sacrificial Writing Into Functional Tissue), microfabrication including patterning, honeycomb scaffold, anisotropic patch, heart on a chip, electronic patch and AngioChip, and hydrogels such as cell encapsulation, casting methods and anchoring supports. [6]

## 1.8. Introducing alignment into engineered cardiac tissues

Cardiac cell alignment, as previously discussed, enhances tissue functionality. This alignment can be achieved using structures such as micropillars, which resist against natural tissue compaction forces, promoting tissue elongation and increased stiffness. The interplay of tissue compaction force and average contractile force for microfeatures can be determined and the design of the microfeatures can be adjusted as desired. [20], [25] Fig. 3 visualizes several cardiac microtissue designs used to study cell alignment, including patches (A and H), rings (B), bundles (C to F), and tubes (G). While rings, bundles and tubes focus on cell analysis and tissue alignment, patches can additionally be easily upscaled, providing a promising cell-based therapy to restore the myocardium. Table 2 summarizes studies that developed microfeature-guided (cardiac) patches (see Fig. 3 H). For instance, Bian et al. [25] explored the effect of microfeature dimensions on cardiac tissue alignment, staining the actin filaments and analyzing the cell orientation. They reported the following findings:

- (i) The local and global cardiomyocyte alignment increases with “increased length/width ratio of the pores.” [25]
- (ii) Changes in the orientation of cardiomyocytes is consistent with changes in the orientation of ECM proteins.
- (iii) Longer pore size increases anisotropic propagation of electrical signals.
- (iv) Increased anisotropic propagation of electrical signals increases contractile force development.

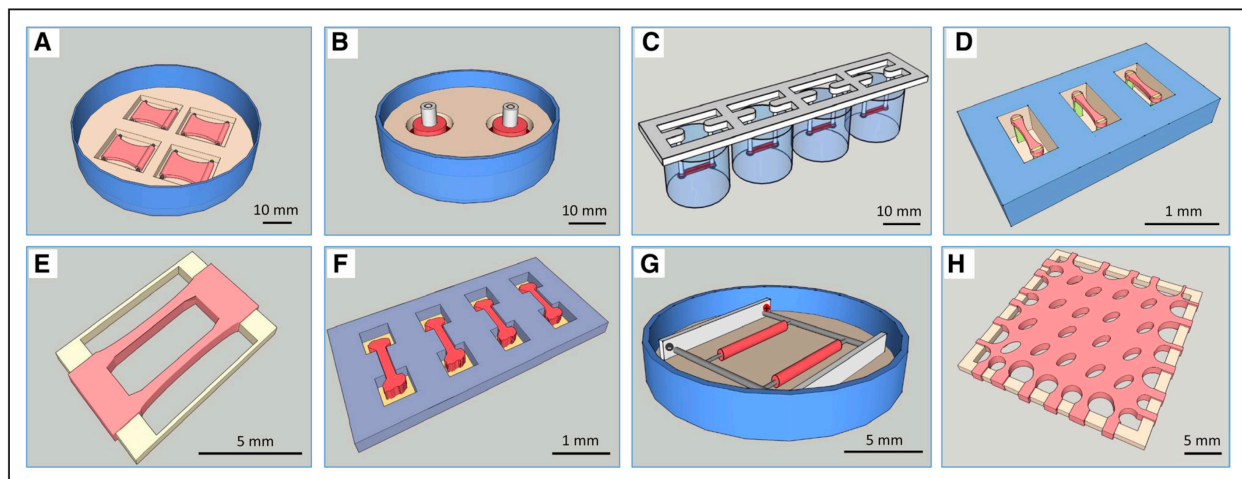


Fig. 3: Engineered heart tissue structures such as a patch (A-H), ring (B), bundles (C, D, E, F) and tubes (G) to study CMs alignment. [10], [26]

Table 2: Literature overview of microfeature guided cell patches including cell type, biomaterials, moulding material, and structural design

<i>Cardiomyocyte cell patch</i>				
<b>Cite</b>	<b>Cell type</b>	<b>Cells and biomaterial</b>	<b>Mould material</b>	<b>Structural design</b>
[27]	Human induced pluripotent stem cell derived cardiomyocytes (hiPSC-CMs)	Cells, fibrinogen and thrombin	Agarose	35 pins (length 2 mm, width 1 mm, height 4 mm)
[28]	hPSC-CMs and human ventricular cardiac fibroblasts	Cells, collagen and Matrigel®	Polydimethylsiloxane (PDMS)	Microfluidic devices with elliptical micropillars
[29]	Isolated CMs from neonatal rats	Cells, collagen I and Matrigel®	Biocompatible MED610 polymer as stiff base and TangoBlack polymer for the flexible poles	3D-printed patch with flexible poles
[30]	Human embryonic stem cell derived cardiomyocytes (hESC-CMs)	Cells, fibrinogen and Matrigel®	PDMS	Elliptical posts (1.2 mm long)
[25]	Neonatal rat ventricular myocytes	Cells, fibrinogen and Matrigel® and thrombin	PDMS	Pillars of 2:1 and 3:1 length: width ratio
[31]	Neonatal rat ventricular myocytes	Cells, fibrinogen and Matrigel® and thrombin	PDMS	Elliptical posts
[32]	Mouse embryonic stem cell derived CMs, cardiovascular progenitors and primary neonatal rat ventricular fibroblasts	Cells, fibrin	PDMS	Elliptical posts
[33]	Neonatal rat skeletal myoblasts	Cells, fibrinogen and Matrigel® and thrombin	PDMS	Elliptical posts
<i>Cell patch (no Cardiomyocytes)</i>				
[34]	Human chondrocytes and Normal human fibroblasts (NHF)	Cells, fibrinogen, Matrigel® and thrombin	Agarose	Uniaxial (dogbone), equibiaxial (trampoline), biaxial (cross), circumferential (toroid), and multiaxial tension (triangle) shape
[35]	Human dermal fibroblasts (HDF)	Cells, collagen I	PDMS	Square, hexagonal, and octagonal shape
[36]	NIH 3T3 cells	Cells, collagen I	PDMS	Square shape

### 1.9. Mould fabrication

It is known that hydrogel-based moulds with microarchitectures can direct cardiac tissue organization into specific structures, such as anisotropic patterns, enhancing tissue function and maturation. There are two main techniques to produce such a microfeature mould. (i) Photolithography and soft lithography, and (ii) Stereolithography (SLA). [20], [25], [37]

(i) In photolithography, microfeatures are etched into a rigid substrate like SU-8/silicon wafer. Either this wafer represents the desired design or soft lithography is used to cast PDMS negative moulds. (ii) SLA, on the other hand, is a 3D printing technique that creates 3D objects from liquid photoresin, a material that solidifies when exposed to UV light. First, a 3D CAD model will be created and sequentially sliced into parallel 2D cross-sections. These 2D slices are projected onto the resin tank to build a layer-by-layer structure. As illustrated in Fig. 4, the SLA printer consists of a tank filled with liquid resin and UV light shines onto a digital micromirror device to create precise 2D images. These images are projected onto the transparent-bottom of the resin tank, solidifying specific areas. Meanwhile, a platform within the tank moves vertically along the Z-axis, allowing the next layer to be formed atop the previous one. [37], [38]

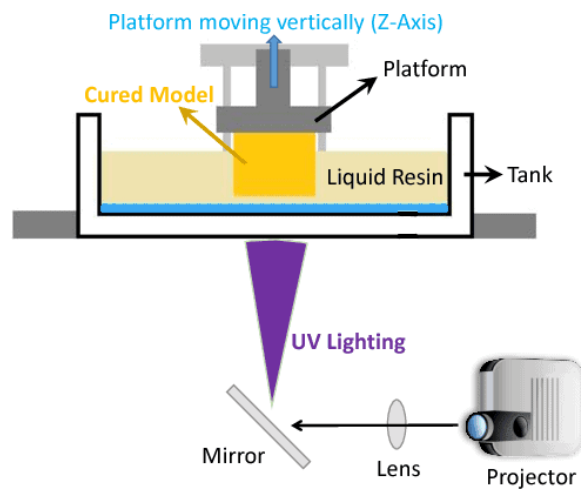


Fig. 4: SLA setup including transparent-bottom tank filled with liquid photoresin, a vertically moving platform and a projector that shines UV light onto a digital micromirror device to project a specific 2D image onto the resin tank, curing precise regions. [38]

### 1.10. Moulding materials

In the literature, non-adhesive, transparent, and biocompatible materials such as (i) PDMS and (ii) agarose are commonly used for seeding cells or spheroids into moulds (see Table 2). Both materials are accessible, easy to handle, and enable cost-effective mould fabrication without requiring complex equipment. (i) PDMS is widely utilized as a master mould for casting materials like agarose for biological experiments. However, PDMS moulds can also be used directly. (ii) Agarose on the other hand, is a natural polysaccharide polymer and is non-toxic, versatile, and easily modifiable, making it well-suited for casting applications. [39], [40], [41]

## 2. Aim and Objective

### *Aim*

The aim of this study is to fabricate a system to control cardiac tissue self-assembly using spheroids as building blocks.

### *Objective*

The first objective of this study is to design and develop a mould suitable for cell culture applications. The mould structure must be evaluated and the mould itself must meet requirements, including biocompatibility, sterilizability, and resistance to cell incubation conditions.

The second objective is to assess, the seeding process and the subsequent fusion of spheroids within the mould, forming a 3D *in vitro* tissue. Finally, the use of mixed cardiac cell spheroids will serve as a proof of concept to validate the system's functionality.

## Materials and Methods

**Materials** Elegoo Saturn 2, Elegoo washing and UV curing machine, Siraya Tech Blu-Tough Clear V2 Resin, Agarose Sigma Aldrich (A9539), T75 flask (SIAL0641), Corning® Elplasia® 12K Flask, Hettich ROTINA 380 Centrifuge, Eppendorf® Thermomixer Compact (RCF=0.0001933 x (RPM)<sup>2</sup>), Branson 200 Ultrasonic Cleaner, Microscope EVOS M5000, Heracell™ VIOS 160i CO<sub>2</sub> Incubator, Luna Automated Cell Counter, Sarstedt 12 well cell culture plate (83.3921), T25 flask (Sarstedt, 83.3910.002), Alexa Fluor™ 488 Phalloidin (ThermoFisher, A12379), DAPI and Hoechst Nucleic Acid Stains (ThermoFisher, 62249)

**Liquids** Fibroblast Growth Medium (116-500), Rat Neonatal Cardiomyocytes (R-CM-561), Hanks' Balanced Salt solution (H6648), 0,025% Trypsin-EDTA solution (T3924), Trypsin inhibitor from Glycine max (soybean, T6414), Freezing Medium Cryo-SFM (C-29912), dPBS, MilliQ-water, Ethanol, Isopropanol, Myocyte Growth Medium (C-22070), Myocyte Growth Medium (C-22070), HEPES Buffered Saline Solution (C-40020), Trypsin Neutralizing Solution (C-41110), Paraformaldehyde, 32% w/v aq. soln., methanol free, Thermo Scientific Chemicals (047377.9L)

### 1. Mould design and fabrication

#### 1.1. CAD design & slicing software

The mould, including the feature base, cup, and holder, was designed in CAD software (Shapr3D, v5.642.0.7078). The models were prepared using slicing software (LycheeSlicer, v6.0.2) and oriented horizontally (0°) for printing with an Stereolithography (SLA) printer (Elegoo Saturn 2). Manufacturer-recommended print settings were applied, with adjustments to layer thickness (20 µm) and exposure times (< 3 s) as described in the results section 1.2 to 1.4.

#### 1.2. 3D Printing (SLA)

Moulds were printed with an SLA printer (Elegoo Saturn 2) using Siraya Tech Blu-Tough Clear V2 photocuring resin. To remove any uncured resin, the moulds were washed in 99% isopropanol for 3 minutes in an Elegoo magnetic stirrer washing station. The feature base underwent an additional 5 minute sonication in fresh 99% isopropanol, and the microfeatures were vacuumed to ensure complete resin removal. All moulds were then dried at 60°C for 20 minutes to evaporate the isopropanol, followed by a 10 minute UV curing in the Elegoo UV curing station. Finally, the moulds were sterilized via dry autoclaving at 121°C for 3 hours.

#### 1.3. Agarose casting

Agarose casting was performed in a laminar flow hood and is visualized in Fig. 5. The moulds (microfeature base and cup) and holder were assembled in a 50 mL tube (2), and a 2 wt% (weight percentage) agarose solution (Sigma Aldrich, Agarose A9539) in Milli-Q water was prepared, sterilized, and stored at 4°C until use. For casting, the agarose was liquefied by heating to 95°C in a heat block (1). Using a wide-opening pipette, 2 mL liquefied agarose was poured into the mould (2) and centrifuged at 700 rpm for 15 seconds (3). Additional 200 µL liquefied agarose were added after centrifuging to compensate for the loss during the process (4). The agarose was then allowed to gel for 10 minutes (5). With sterile tweezers and a spatula, the solidified agarose was carefully removed from the resin mould, creating a negative copy, and stored in Milli-Q water at 4°C until use (6 to 8).

Before cell exposure, the pH of the agarose moulds was equilibrated by incubating them twice in cell culture media for 20 minutes (at 37°C, 0.5% CO<sub>2</sub>).

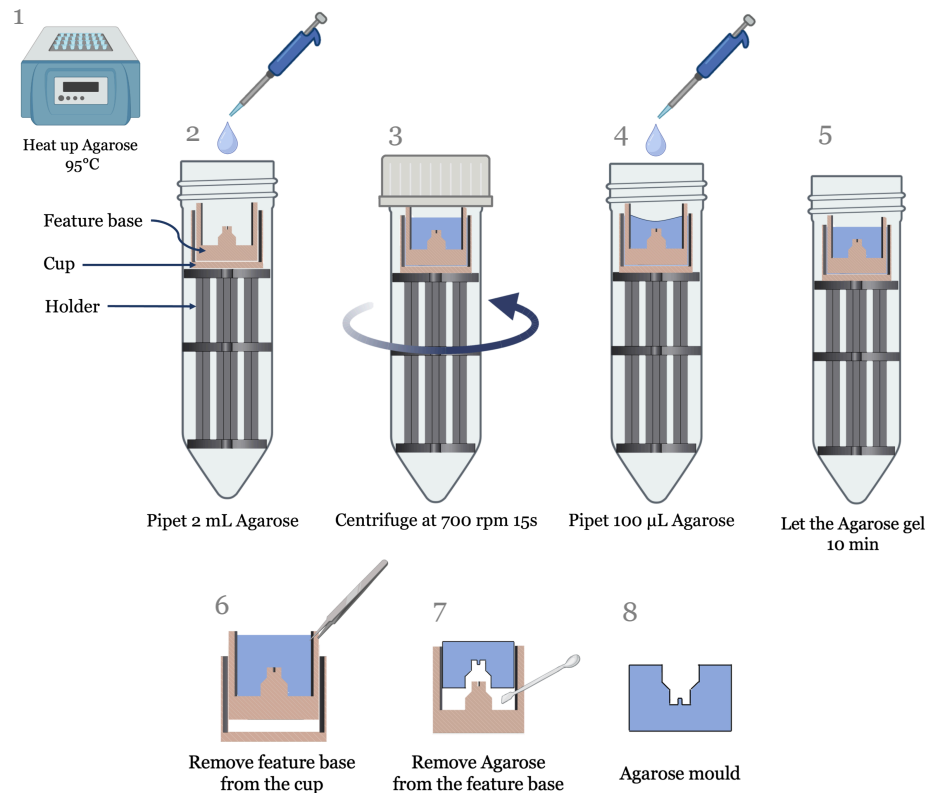


Fig. 5: Agarose casting method starting with heating up agarose to 95°C (1) and assembling the microfeature base, the cup and the holder into a 50 mL tube (2), then centrifuging at 700 rpm 15s (3), add 100 µL agarose (4), letting it gel for 10 minutes (5) and remove the agarose mould from the resin mould using tweezers and a spatula (6 to 8). [42]

#### 1.4. Micro-engineering features

The agarose mould contains in total seven elliptical microfeature pillars, all with a design width of 0.5 mm. Five pillars have a length of 2 mm and two pillars a length of 1.2 mm. The pillar height design is either 0.5 mm or 1 mm.

## 2. Cell culture and spheroid formation

### 2.1. Fibroblast and cardiomyocyte cells culture

Human Dermal Fibroblasts (HDF, adult, 106-05A) were thawed and seeded into a T75 flask (SIALO641) (255.000 cells and 15 mL Fibroblast Growth Medium 116-500) and cultured till 80% confluent and passaged once until used. The passage was done by washing the cells with 5 mL Hanks' Balanced Salt solution (H6648), then adding 3 mL 0,025% Trypsin-EDTA solution (T3924), covering the whole surface and removing 2.5 mL. After about 2 minutes, when the cells detached, 2 mL Trypsin inhibitor from Glycine max (soybean, T6414) were added. The cells were collected and centrifuged at 220 rpm for 5 minutes. The supernatant was removed and Fibroblast Growth Medium (116-500) was added to reseed the cells into a T75 flask (SIALO641) (255.000 cells and 15 mL Fibroblast Growth Medium 116-500) and paced into the incubator (37°C, 0.5% CO<sub>2</sub>) or to use for experiments (see method section 2.2 to 3.1). Cell media was changed very other day.

Rat neonatal cardiomyocytes (rat CM, R-CM-561) were thawed and seeded into a T25 flask (Sarstedt, 83.3910.002) at a density of 2 million cells in 7 mL of Myocyte Growth Medium (C-22070). The cells were cultured for two weeks and passaged once during the period. For passaging, cells were washed with 5 mL of HEPES Buffered Saline Solution (C-40020) and detached adding 1 mL of 0.04% Trypsin-EDTA solution (T3924). After detaching, 2 mL of Trypsin Neutralizing Solution (C-41110) was added, and the cell were centrifuged at 220 rpm for 5 minutes. After removing the supernatant, the cells were resuspended in Myocyte Growth Medium (C-22070) for spheroid production (see method section 2.2).

## 2.2. Spheroid production

To produce spheroids with a cell concentration of approximately 1000 cells (HDF only or HDF with rat CMs (1:1 ratio)), two methods were used, either a Corning® Elplasia® 12K Flask or 2 wt% agarose moulds made by MicroTissues® 3D Petri Dishes® (MTPD® [43]).

For the Corning® Elplasia® 12K flask, the flask was prewetted using 10 mL of 70% ethanol, 15 mL water, and 10 mL dPBS. Then, the flask was filled with 20 mL of cell culture media and incubated at 37°C with 0.5% CO<sub>2</sub> until used. Cells were trypsinized, counted with the Luna automated cell counter, and seeded at a density of 12 million cells in 10 mL of media. The total media volume in the flask was thereby 30 mL. The flask was incubated for 3 to 4 days in a horizontal position (at 37°C with 0.5% CO<sub>2</sub>) and cell media was changed every other day. To collect the spheroids, the flask was placed in a vertical position and the cell media including the spheroids were collected and centrifuged at 70 rpm for 3 minutes. After removing the supernatant, spheroids were either used directly for seeding experiments by adding 100 µL per 1000 spheroids or diluted in Freezing Medium Cryo-SFM (C-29912) (about 1000 spheroid in 1 mL) and stored at -80°C for up to six weeks, or in liquid nitrogen for long-term storage.

For the MTPD®, moulds and 2 wt% agarose were sterilized before use. Liquefied agarose (heated to 95°C, as described previously) was poured into the MTPD® moulds using wide-opening pipette tips and left to gel. Then, the agarose moulds were collected and stored in Milli-Q water at 4°C. Before usage, the moulds were equilibrated as described in method section 1.3. Afterwards, a cell concentration of 1000 per microwell was seeded onto the moulds and allowed to settle for 20 minutes. 2 mL of cell media was added sequentially, and the moulds were incubated for 3 to 4 days and media replaced every other day. To collect spheroids, the cell media was removed, and 1 mL of fresh media was added. The moulds were then flipped using a sterile spatula and centrifuged at 70 rpm for 3 minutes. In case spheroids did not detach, media flushing was used to release them. Collected spheroids were centrifuged again at 70 rpm for 3 minutes and the supernatant was removed. The spheroids were either used immediately or frozen as previously described.

## 3. Spheroid fusion and tissue analysis

### 3.1 Seeding spheroids in self-designed and developed moulds

Spheroids were either used immediately after spheroid production or thawed by partially immersing the vial in a 37°C water bath until a small ice fragment remained. The vial was then transferred to a laminar flow hood, and 1 mL of cell-associated medium was added. Spheroids were collected in a falcon tube, centrifuged at 70 rpm for 3 minutes to remove the supernatant. Then, cells were resuspended in fresh medium at a concentration of 1000 spheroids per 100 µL. To know the precise spheroid concentration, a wide-opening pipette was used to collect 20 µL of spheroid suspension for counting and diameter measurement using the Microscope EVOS M5000. *Equation 1* was used to calculate the seeding volume and a wide opening pipet was used to seed the spheroids into the seeding area of the mould. Spheroids were left to settle for 5 minutes, and the seeding distribution was checked microscopically. Adjustments were made by adding more spheroids to cover the whole seeding area if necessary or tapping the well plate to distribute the spheroids homogeneously.

$$d_{sph} [mm] = \text{Average spheroid diameter } [\mu m] * 10^{-3}$$

$$\text{Spheroid area } [mm^2] = \pi * \left( \frac{d_{sp} [mm]}{2} \right)^2$$

$$\text{Spheroids per } \mu L \left[ \frac{1}{\mu L} \right] = \frac{\text{Spheroids counted}}{\text{Droplet volume } [\mu L]}$$

$$\text{Spheroid seeding area } [mm^2] = 2 * \text{Mould seeding area } [mm^2] = 2 * 10.67 mm^2 = 21.34 mm^2$$

$$\text{Seeding volume } [\mu L] = \frac{\text{Spheroid seeding area } [mm^2]}{\text{Spheroid area } [mm^2]} * \frac{1}{\text{Spheroids per } \mu L \left[ \frac{1}{\mu L} \right]}$$



Equation 1:

$$\text{Seeding volume } [\mu\text{L}] = \frac{21.34 \text{ mm}^2}{\pi * \left(\frac{d_{sph} [\text{mm}]}{4}\right)^2} * \frac{\text{Droplet volume } [\mu\text{L}]}{\text{Spheroids counted}}$$

### 3.2 Analysis

#### *Spheroid compaction, circularity and fusion level*

To analyze spheroid compaction, images were captured at 20 minutes, 24, 48 and 72 hours using a 4x objective of the Microscope EVOS M5000. A mask was created using a Trainable Weka Segmentation (v3.3.4) in ImageJ2, applying automatic thresholding and analyze particles to measure spheroid area and perimeter. The area over time describes the compaction while the circularity was calculated as following:

$$\text{Circularity} = \frac{4 * \pi * \text{Area } [\text{mm}^2]}{(\text{Perimeter } [\text{mm}])^2}$$

The fusion level was determined by measuring the maximal and minimal length of the two spheroids when positioned next to each other at time point 0 hours and 24 hours. The fusion level is the quotient of minimal to maximal length.

#### *Tissue compaction*

To analyze spheroid fusion, images were captured at 3, 6, 9, 12, 24, and 48 hours using a 4x objective of the Microscope EVOS M5000. Images from each sample were stitched in ImageJ2 (v2.14.0/1.54f) using Grid/Collection Stitching with parameters based on Preibisch et al. (2009), including linear blending, a regression threshold of 0.30, displacement thresholds of 2.50 (max/avg) and 3.50 (absolute). Tissue compaction over time was analyzed with Trainable Weka Segmentation (v3.3.4) in ImageJ2, applying automatic thresholding and analyze particles to measure the tissue area.

### 3.3 Histological analysis

Samples were washed three times with sterile dPBS, then fixed in 10% Paraformaldehyde (PFA) at 4°C for at least 24 hours before histology processing. H&E staining was performed, and images were captured using a colorimetric camera with a 4x magnification. ImageJ2 was used to stitch images together as mentioned previously. The tissue dimensions were determined, creating a segmentation as previously described using ImageJ2 and measuring the minimal and maximal length of the objective.

### 3.4 Fluorescent labeling of cellular structures

#### *Staining and image acquiring*

The samples were fixed with 4% PFA for 30 minutes and washed three times with dPBS. Then cells were permeabilized using 0.1% Triton X-100 for 15 minutes, washed twice with dPBS, and stained with Alexa Fluor™ 488 Phalloidin (ThermoFisher, A12379) (1:300) and Hoechst Nucleic Acid Stains (ThermoFisher, 62249) (1:2000) in dPBS for 2 hours. After staining, again, samples were washed twice with dPBS and imaged using EVOS M5000 microscope (4 and 10x objective).

#### *Image processing*

For processing the images, Imaris (v10.01) was used. A background subtraction and deconvolutions were performed. Additionally, ImarisStitcher (v10.2.0) was used to stitch the images that were taken using the 4x objective of the EVOS M5000 microscope. For visualization, the same light intensity settings were used for the same magnification.

# Results

The results show the design and development of microfeature agarose moulds and the analysis of spheroid production, seeding, fusion as well as cell alignment. Key methods to analyze tissue formation were area measurement at different conditions (photoresin) or time points (tissue compaction), histology and fluorescent labeling. The results provide insights into print setting optimizations of an SLA printer, the impact on spheroid seeding densities on tissue formation and the relationship between microfeature as structural barriers, spheroid coherence and cell alignment.

## 1. Mould fabrication

### 1.1 Cardiac patch mould requirements

To design a cardiac patch mould, specific requirements have to be taken into account such as mould material, fabrication and cells specific requirements. Those can be seen in Table 3.

Table 3: Cardiac patch mould requirements [44]

Mould material	<ul style="list-style-type: none"><li>- Biocompatible</li><li>- Sterilizable</li><li>- Mechanical integrity:<ul style="list-style-type: none"><li>- Withstand tissue compaction and continuous stretching/relaxing motion of the myocardium</li><li>- No degradation during culture time</li></ul></li></ul>
Mould fabrication	<ul style="list-style-type: none"><li>- Material must be easily accessible</li><li>- Designed with acceptable cost</li><li>- Easily adaptable</li><li>- Cell measuring systems integrable</li><li>- Sterile mould production</li><li>- Allow tissue release</li></ul>
Cardiomyocyte specific	<ul style="list-style-type: none"><li>- Support cell alignment</li><li>- Support cell maturation</li></ul>

## 1.2 Microfeature printability

A design to explore microfeature resolution of the 3D printer can be seen in Fig. 6 A. The design of the holes was based on a paper and protocol of Bian et al. [3], [25], as it focused on the anisotropy of engineered cardiac tissue, varying the size, spacing and elongation of elliptical pillars. In Fig. 6 A, the hole dimensions ranges from 0.2 to 0.5 mm in width (0.05 mm steps), 0.8 to 2.0 mm in length (0.2 mm steps), and 0.6 to 1.2 mm in depth (0.4 mm steps). Four hole dimensions (highlighted in Fig. 6 A) were selected to analyze the effect of varying the exposure time on the hole width, length and depth. Fig. 6 B shows the holes after printing, washing and UV curing.

The hole area design of number (no.) one and four are the same (0.875 mm<sup>2</sup>) but they vary in hole depth: no. one of 1 mm depth and no. four of 0.6 mm depth. Design no. two and three, both have a hole depth of 1 mm but differ in hole dimensions: no. two is shorter in length (hole area of 0.288 mm<sup>2</sup>) and no. three is shorter in width (hole area of 0.380 mm<sup>2</sup>). Fig. 6 C and D compares the impact of the exposure time at 1.4s, 1.8s and 2.2s on different hole areas at the same depth (C) and different depth at the same area (D). Therefore, design no. one is visualized in both graphs and both graphs show a decrease in hole area with increased exposure time.

The linear equations in Fig. 6 C show, the impact of the exposure time is four times higher for no. two and 3 times higher for no. three compared to no. one. This indicates, the effect of the exposure time increases with decreased hole areas. Interestingly, based on the linear equations of Fig. 6 C, increasing the hole depth (no. one), increases the exposure time impact by 2.24 compared to a lower hole depth (no. four), resulting in a worse fidelity for deeper holes. However, when comparing the progression line at single exposure times, the effect is lower at lower exposure times (1.4s: 1.04 times, 1.8s: 1.05 times, 2.2s: 1.21 times).

Based on the results, to increase the fidelity the following parameters can be changed: decreasing the exposure time, increased the hole area and/ or decreasing the hole depth. For further experiments, the largest feature area design (no. one and four) will be taken forward, not only because of the increased fidelity at higher exposure times but mainly because the design corresponds to the highest length width pillar ratio mentioned in Bian et al. [3], [25] The optimal mould exposure time will be explored separately, as changing the mould design influences the print resolution (see results section 1.4).

Additionally, a print angle of 0° and 45° were tested and can be seen in Fig. 6 E and F (design no. one, exposure time 2.2s). While a print angle of 0° causes a hole free from cured resin and resulting in good fidelity, the feature printed with a 45° angle, shows undesired cured resin and a ribbed surface, resulting in a bad fidelity. As a result, the mould will be printed in a 0° print angle.

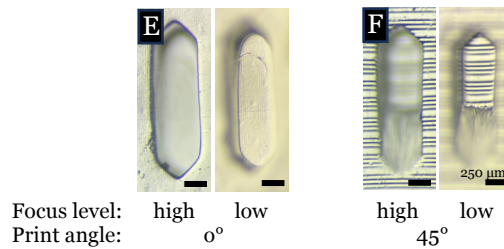
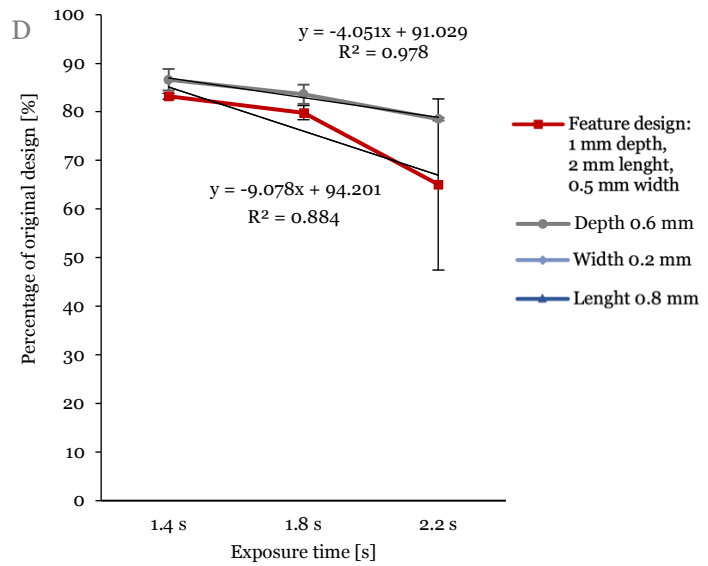
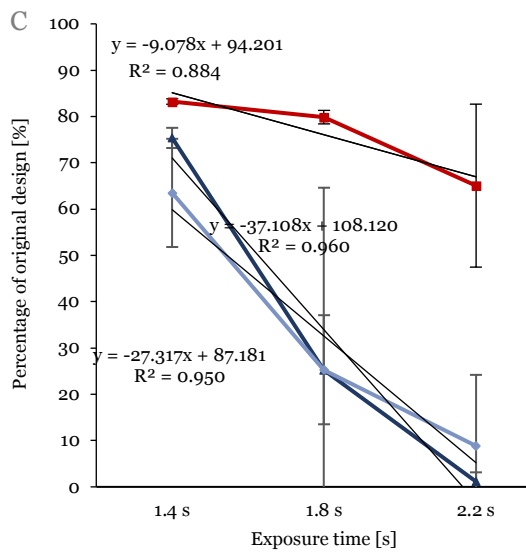
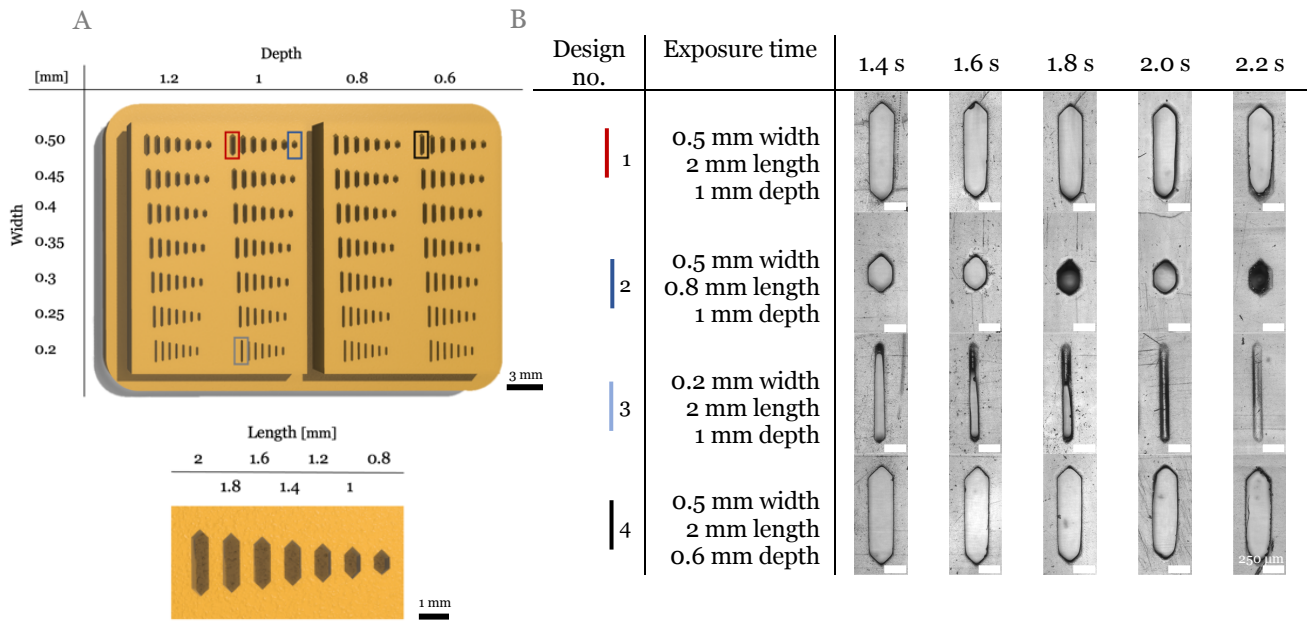


Fig. 6: Resin design to explore microfeature resolution (A), Microscopic images (4x object) of selected resin holes after printed, washed and UV cured (no. 1: 0.5 mm width, 2 mm length, 1 mm depth, no.2: 0.5 mm width, 0.8 mm length, 1 mm depth, no. 3: 0.2 mm width, 2 mm length, 1 mm depth and no. 4: 0.5 mm width, 2 mm length, 0.6 mm depth) (B), UV light exposure time effect on resin hole area of different feature dimensions (no. 1, 2 and 3)) (C) and UV light exposure time effect on resin hole area of different feature depth (no. 1 and 4) (D). Print angle of 0° (E) and 45° (F) of design no. 1, exposure time 2.2. Three replicates from one independent experiment. Graph show  $\pm$  Standard Deviation (SD). Unmarked scale bar 250  $\mu$ m.

### 1.3 Mould design

The microfeatures design of 0.5 mm width and 2.0 mm length was selected from the previous results section 1.2 (design no. one and four) and can be seen in Fig. 7 A. The pillars dimensions, pillar-to-pillar and pillar-to-wall distance are designed to seed spheroids of approximately 200  $\mu\text{m}$  in diameter, allowing two spheroids to be positioned next to one another and stacked vertically (hole depth: 0.5 and 1 mm). The seeding area is 10.67  $\text{mm}^2$  and the microfeatures are placed on a 6 mm platform to create a cavity in the agarose mould for 100  $\mu\text{L}$  spheroid seeding media.

The mould consists of two parts, the feature base (including the microfeatures on a platform, Fig. 7 B) and the cup (Fig. 7 C). The mould assembled can be seen in Fig. 7 D, where the feature base is placed into the cup. Thereby, two pillars at the side of the feature base function as a tool to remove the feature base from the cup after agarose casting. Two cavities at the side of the feature base allows a better grip with tweezers during release of the agarose mould from the resin. The vertical distance between the seeding area (microfeatures) and the top of the cup is 4.7 mm, to ensure the agarose mould does not exceed the working distance of the microscope (6 mm). Technical drawings can be seen in the appendix.

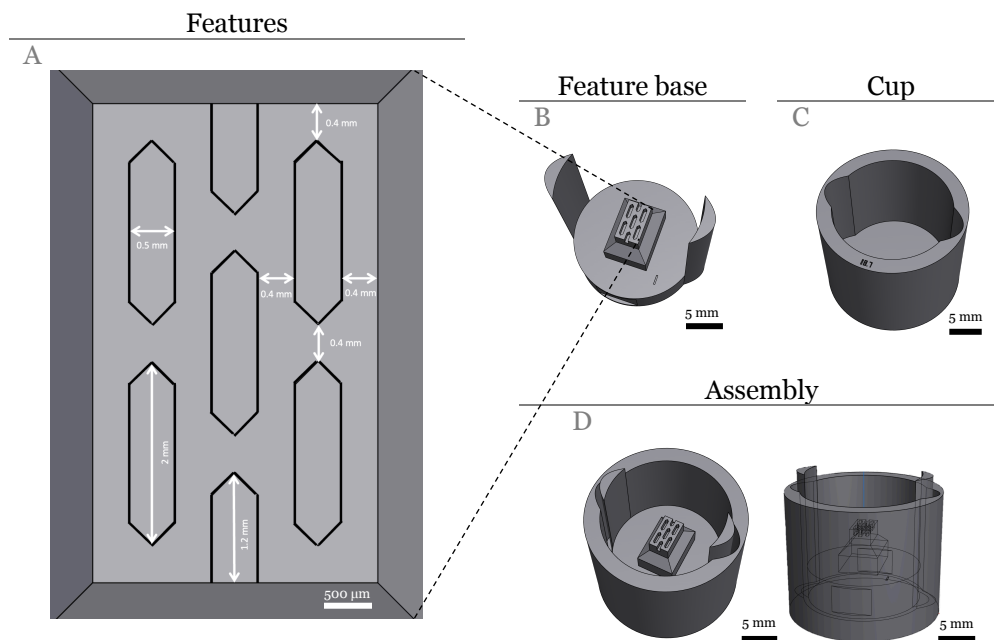


Fig. 7: Mould design incusing microfeature design of 2 mm length and 0.5 mm width (A), mould feature base (B) and mould cup (C). The assembly of the feature base and the cup (D).

## 1.4 Mould design printability

As mentioned in results section 1.2, decreasing the exposure time, increases the hole area. This effect can also be seen in Fig. 8.

Fig. 8 A shows, the analysis of hole area of microfeatures with a hole depth of 0.5 mm (Fig. 8 B to D). The linear equation ( $y = -0.07x + 0.70$ ) indicates, the hole area decreases with increasing exposure time (2.2s is 74.66%, 2.4s is 56.47% and at 2.6s is 57.74% of the design).

Comparing the resin microfeatures at different hole depth and same exposure time of 2.2s, then it can be seen, while a depth of 0.5 mm has clear features, the resin mould with a depth of 1 mm has cured resin within the microfeature reducing the fidelity (see Fig. 8 B and K at exposure time 2.2s). Thereby, increasing the hole depth decreases the fidelity, which coincides with the results of results section 1.2.

To explore agarose casting, two resin mould designs are taken forward: (i) a hole depth of 0.5 mm at an exposure time of 2.2s and (ii) a hole depth of 1 mm exposure time 1.0s. Those were chosen as the exposure times create microfeature holes free from undesired cured resin (Fig. 8 B and E).

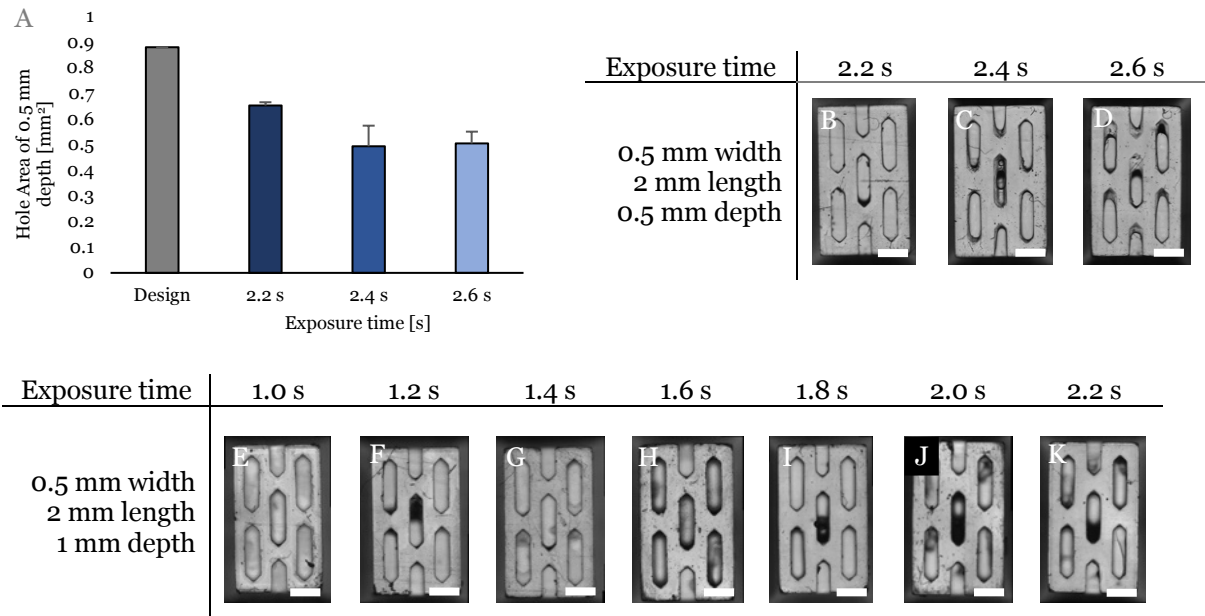


Fig. 8: The mould design fidelity analyzed (A) of resin mould with a hole depth of 0.5 mm at exposure time 2.2 (B), 2.4 (C) and 2.6s (D). The resin mould with a hole depth of 1 mm at exposure time 1.0 (E), 1.2 (F), 1.4 (G), 1.6 (H), 1.8 (I), 2.0 (J) and 2.2s (K). Three replicates from one independent experiment. Graph show  $\pm$  SD. Scale bar is 1 mm.

## 1.5 Agarose casting

When pouring agarose on to the resin mould, air bubbles are trapped between the resin mould and the liquid agarose. The effect increases with increasing hole depth (see Fig. 9 C and I).

To overcome this, two methods were explored, centrifuging and vacuuming. For vacuuming, a challenge was to remove the air bubbles from the agarose mould and to create a sterile environment. This was not a challenge when centrifuging. However, a mould holder was required to better access the mould for pouring agarose, as well as to keep the mould flat during centrifuging and gelation time (see Fig. 9 N). The mould and holder assembled in a 50 mL falcon tube can be seen in Fig. 9 M.

Fig. 9 also shows the effect of air bubble release at different centrifuging speeds (500, 700, 1000 rpm). It can be observed that air bubbles are trapped, when centrifuging at 500 rpm (D and J), but at 700 (E and K) and 1000 rpm (F and L), the air bubbles are released.

Furthermore, due to the centrifuge force, agarose was removed from the cup, creating a meniscus, when gelling. To reduce the effect, the pulling pillars were moved from the top of the feature base (see Fig. 9 B) to the side, crating a circular agarose mould (see Fig. 9 H and G). To decrease the meniscus even further, after centrifuging and before agarose gelation, additional 200  $\mu$ L liquid agarose gets poured into the cup. The final outcome can be seen in Fig. 9 O to Q. It shows the mould assembly from the side (O) and top including gelled agarose (P) as well as the agarose mould with a pillar height of 1 mm, centrifuged at 700 rpm and casted from the resin mould of pulling pillars at the side, creating a circular mould (Q).

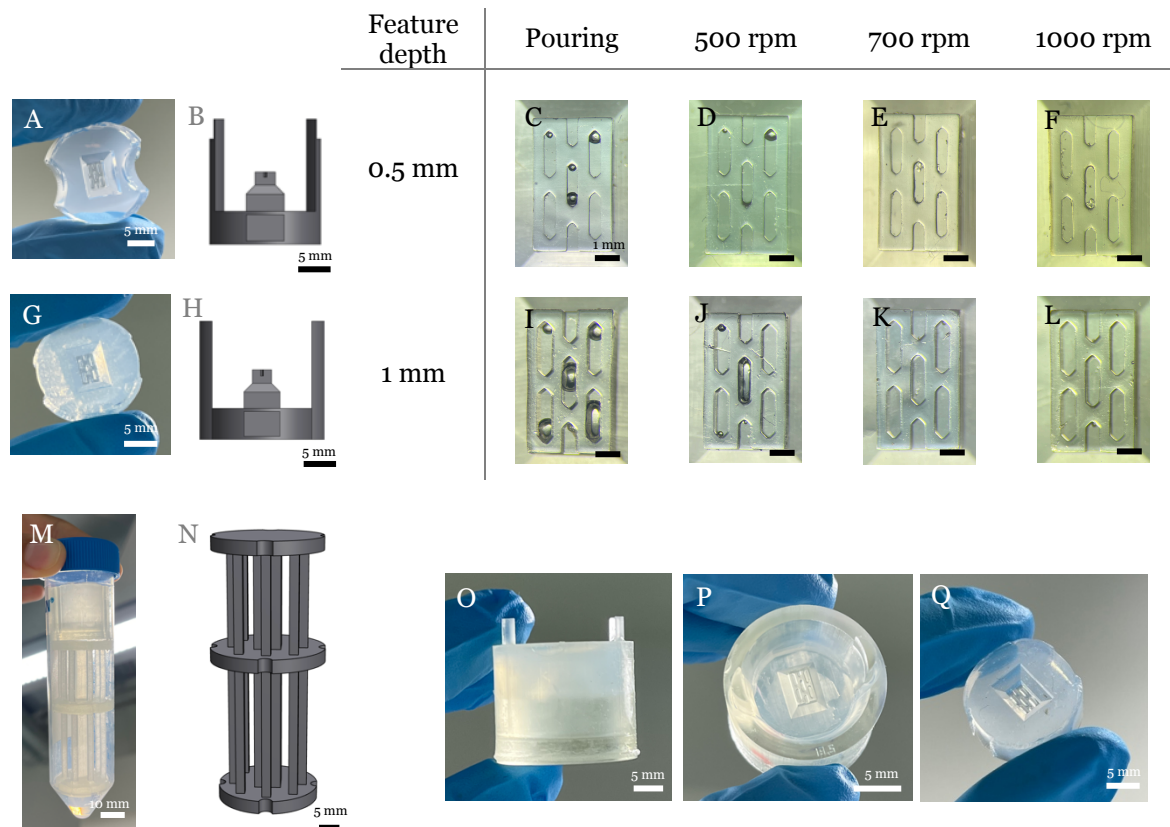


Fig. 9: Quality of agarose casting for hole depth of 0.5 and 1 mm without (pouring) and with centrifuging at different rpm (500, 700 and 1000 rpm) (C to F and I to L). Mould design and agarose mould of hole depth of 0.5 mm (A and B) and for 1 mm depth (G and H). The holder (N) and the mould with holder assembled in a 50 mL falcon (M). The mould assembly from the side (O) and top including gelled agarose (P) and the agarose mould with a pillar height of 1 mm (Q).

## 1.6 Comparison of design, resin, and agarose moulds

Fig. 10 shows the microfeature design (A), the printed resin mould (positive, holes) (B), and the agarose mould (negative, pillars) (C). Graph D compares the area of those three and results in a resin hole area of 91%, and the agarose pillar area of 78% of the design. Graph E represents the hole depth and pillar height vs the design, which is 97% for the resin and 98% for the agarose.

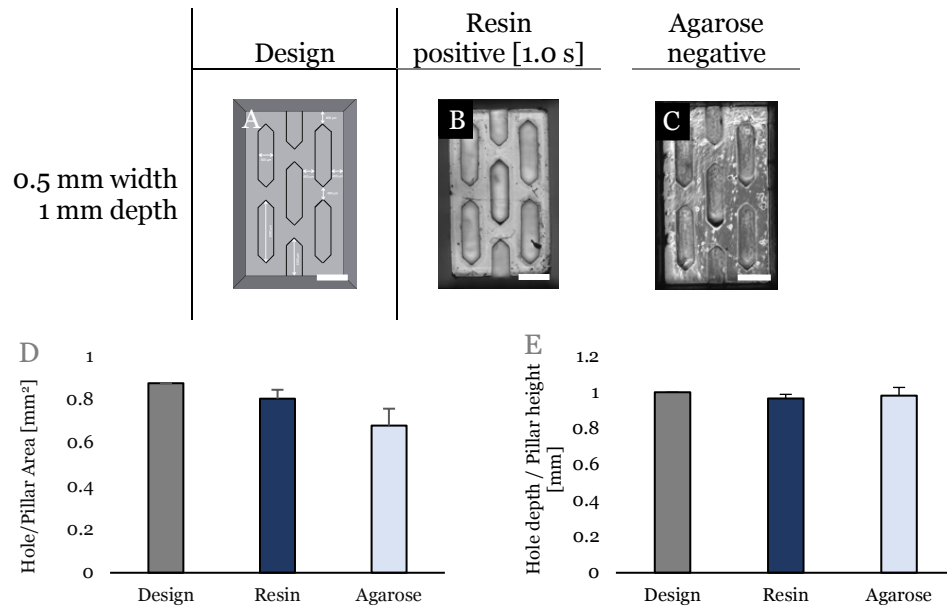


Fig. 10: Resin design (A), print (B) and agarose mould (C), Hole/ Pillar area [mm<sup>2</sup>] (D) and height [mm] (E). Three replicates from one independent experiment. Graph show  $\pm$  SD. Scale bar 1 mm.



## 2. Spheroid compaction

HDF spheroid compaction was measured over time including spheroid area at 20 min, 24, 48 and 72 hours and circularity at 24, 48 and 72 hours (see Fig. 11 A to D). Graph E visualizes the spheroid area and the circularity over time and shows, within the first 24 hours, the spheroid area decrease is the greatest, with more than 70%. Afterwards, the area decreases by around 20% and 18% every 24 hours. On the other hand, the circularity increases over time showing a 2.4 increase comparing 24 hours and 48 hours and a 1.2 increase comparing 48 hours and 72 hours. Both, spheroid area and circularity show an exponential progression, by creating the largest effect within the first 24 hours of measuring and decreasing over time. As a result, HDF spheroids at culture day three are used for initial mould experiments, as they formed circular compacted spheroids.

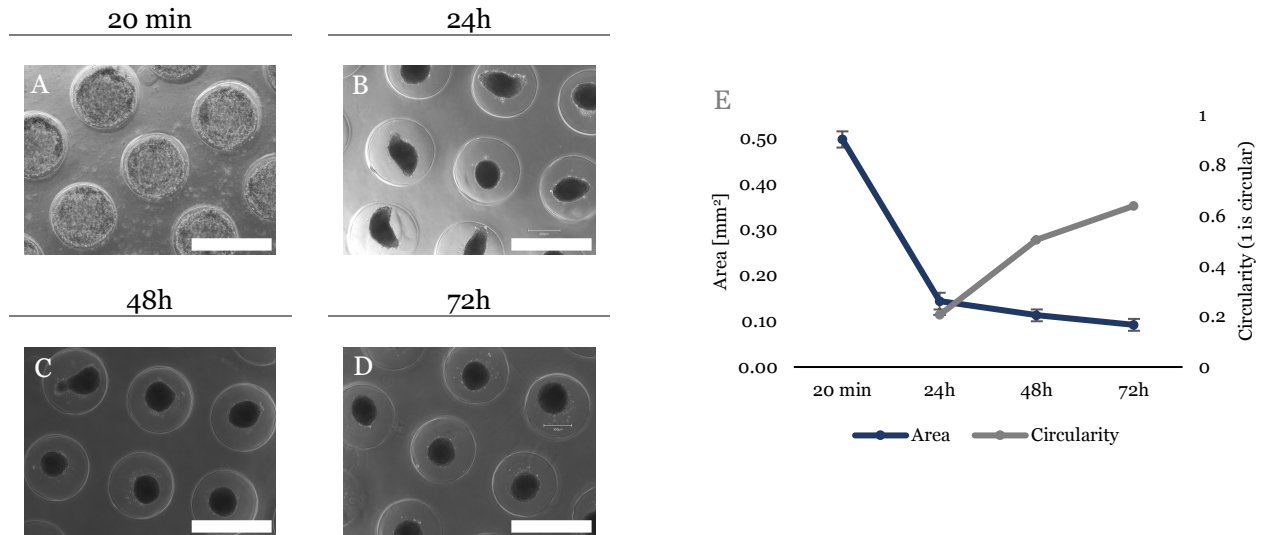


Fig. 11: HDF spheroid compaction over time (20 min, 24h, 48h, 72h) (A), Spheroid area and circularity analysis over time (24h, 48h, 72h) (B). Four to six replicates from one independent experiment. Graph show  $\pm$ SD. Scale bar is 1 mm.

### 3. Spheroid fusion

To determine if the agarose mould fabrication can produce moulds for cell culture experiments at test was conducted: agarose moulds casted from self-designed resin moulds (see Fig. 12 D) were compared to commercially available silicon moulds (MTPD® [43], Fig. 12 A). The fusion behavior of two single HDF spheroids with a pre-culture time of three days (HDF 3) was analyzed based on circularity and fusion level at time point 0 and 24 hours (see Fig. 12 B, C, E, F and G). Graph G visualizes the circularity and the fusion level of spheroid fused in MTPD® (circularity:  $y = 0.27x + 0.32$ , fusion level:  $y = 0.60x - 0.35$ ) and self-designed moulds (circularity:  $y = 0.34x + 0.18$ , fusion level:  $y = 0.59x - 0.44$ ). Even though, the MTPD® started with a slightly higher circularity (0.07) both, the MTPD® and the spheroid seeded in the self-designed mould end up with the same circularity value of 0.86.

The fusion level shows a similar trend of 0.60 using MTPD® and 0.59 using self-designed agarose moulds within 24 hours. As both agarose moulds, create successful spheroid fusion with similar results, the fabrication of self-designed agarose moulds can be evaluated as sterile and resistant to cell culture conditions while not effecting cell behavior, taking this forward to seeding HDF spheroids into the microfeature moulds.

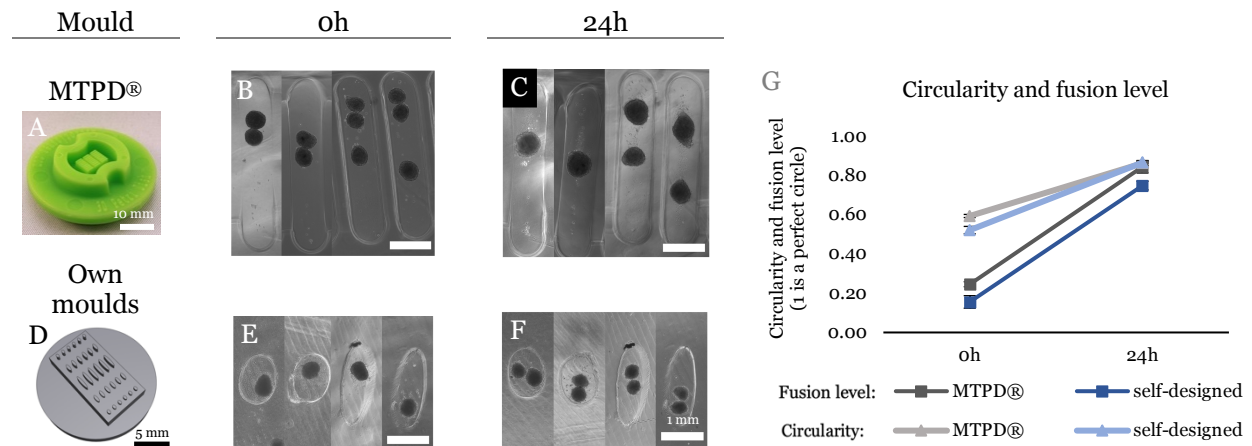


Fig. 12: Two single HDF 3 spheroids seeded in agarose moulds casted from MTPD® [43] (A to C) and self-designed resin moulds (D to F) at time point 0 and 24 hours. Spheroid fusion analysis of circularity and fusion level at 0 and 24 hours (G). Four replicates from one independent experiment. Scale bars are present but too small to be visible. Unmarked scale bar 1 mm.

## 4. Microtissue

### 4.1. Spheroid seeding requirements for homogeneous tissue fusion

The spheroid seeding for self-designed and developed agarose moulds was explored and optimized using HDF spheroids of pre-culture day three (HDF 3, see Fig. 13). Initial experiments can be seen in Fig. 13 A to E, were 300 spheroids, each with a diameter of about 200  $\mu\text{m}$ , were seeded. The spheroids clustered and stacked on top the 0.5 mm high pillars, creating one single tissue fusion, which was not formed around the agarose structures as desired. To improve the tissue formation, the pillar height was increased to 1 mm (Fig. 13 F to W).

When comparing Fig. 13 A to E (pillar height 0.5 mm) and Fig. 13 F to K (pillar height 1 mm), both seeding the same number of spheroids but different diameters (175 and 200  $\mu\text{m}$ ), a difference in seeding area coverage can be observed. Larger spheroids (Fig. 13 A to E) cover a greater seeding area (7.20  $\text{mm}^2$  at 3h), leading to the formation of a single fused tissue after 24 hours. In contrast, smaller spheroids in Fig. 13 F to K covered a smaller seeding area initially (4,00  $\text{mm}^2$  at 3h), leading to the formation of multiple smaller fused tissues after 24 hours.

Further experiments (Fig. 13 F to W) explored the effects of changing the spheroids seeding density (175  $\mu\text{m}$  spheroid diameter). Seeding 300 spheroids produced several small tissue fusions (area reduction of 63.24% in 48h, Fig. 13 F to K). Increasing the density to 600 spheroids resulted in one single tissue (area reduction of 39.56% in 48h, Fig. 13 L to Q), which, however, did not cover the whole seeding area (see Fig. 13 Q). Seeding 900 spheroids created also a single fused tissue (area reduction of 64.26% in 48h, Fig. 13 R to W), but this tissue detached from the agarose pillars after 24 hours (Fig. 13 V) like the tissue in Fig. 13 D. This experiment highlights the need for optimizing the spheroid seeding density, increasing the pillar height even further and/ or adjusting the spheroid pre-culture time. Nevertheless, based on these results, a spheroid seeding formula was established to calculate the seeding volume based on spheroid diameter and concentration stating a negative correlation between those two values.

Interestingly, Fig. 13 X visualizes the reduction in tissue area over time and at 6 hours a shift in tissue area appears, where there is an increase for all samples. Through observation, the gaps between single spheroids began to close within 6 hours without a larger change in overall area reduction (see Fig. 13 H, N and T). Afterwards, the tissue area decreased in a consistent linear progression creating smooth edges (see Fig. 13 E, K, Q and W).

Additionally, it can be observed that the two samples that detached from the agarose structure (Fig. 13 E and W), follow a similar trend of tissue area reduction at time point 9, 24 and 48 hours (Fig. 13 E, 0.5 mm pillar height, 300 spheroids seeded:  $y = -1.83x + 8.60$ , Fig. 13 W, 1 mm pillar height, 900 spheroids seeded:  $y = -1.94x + 8.70$ ).

HDF spheroids with a pre-culture of three days (HDF 3)

Pillar height [mm]	Spheroid		Time					
	Diameter [ $\mu\text{m}$ ]	Amount	0h	3h	6h	9h	24h	48h
0.5	200	<u>300</u>	A	B	C	/	D	E
1	<u>300</u>	<u>600</u>	F	G	H	I	J	K
			L	M	N	O	P	Q
			R	S	T	U	V	W
	<u>900</u>	<u>600</u>						

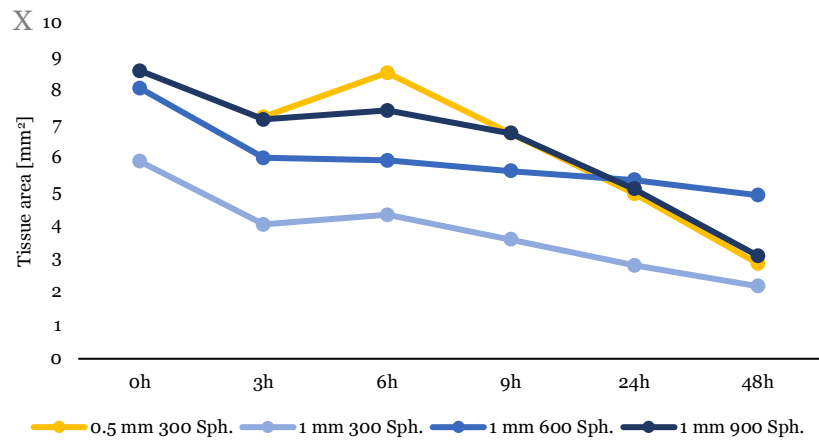


Fig. 13: HDF spheroid seeding densities analysis (X). Agarose pillars of 0.5 mm height and a spheroid seeding density of 300 (A to E). Agarose pillars of 1.0 mm height and a spheroid seeding density of 300 (F to K), 600 (L to Q) and 900 (R to W) at timepoint 0, 3, 6, 9, 24 and 48 hours. One replicate from one independent experiment. Scale bar is 1 mm.

#### 4.2. Exploring spheroid pre-culture time for tissue fusion

One option to manipulate the tissue fusion is by changing the spheroid pre-culture time, therefore in this experiment, HDF spheroids with a pre-culture time of four days (HDF 4) were used. In Fig. 14 A, 1000 spheroids were seeded with a diameter of about 160  $\mu\text{m}$ . This seeding is based on the previous experiment, which showed, reduced spheroid diameter causes the need for increased spheroid amount. However, Fig. 14 A to J shows the tissue fused around the microfeatures over time (0 to 48h), resulting in a single tissue. The tissue area decrease over time can be observed in Fig. 14 K and shows the strongest decrease within the first six hours. Afterwards the reduction stays within 1.5% (3h: 18.44%, 6h: 6.02%, 9h: 0.31%, 24h: -0.78%, 48h: 1.43%), resulting in a total decrease of 24.09% after 48 hours, creating an exponential progression.

Further, Fig. 14 L already gives an indication of the tissue fusion and spheroid cohesion after 48 hours. In the middle of the tissue, single spheroid can be seen, implemented within the tissue structure (red arrows). This part is also lighter compared to the periphery of the tissue, where no or less single spheroid can be observed.

To determine the tissue thickness and better understand the spheroid cohesion, histology was performed, which can be seen in Fig. 14 M to O (nuclei in purple and extracellular structure in pink). In two cross-sections (Fig. 14 M and N), the tissue thickness can be observed and ranges in Y direction from 65  $\mu\text{m}$  to 117  $\mu\text{m}$  and in X direction from 52  $\mu\text{m}$  to 166  $\mu\text{m}$ . Having in mind, that the seeded spheroids had an average diameter of 160  $\mu\text{m}$  prior seeding, tissue compaction occurred which coincides with the tissue compaction analysis of Fig. 14 K. Additionally, a reduction in tissue thickness in the center compared to the periphery can be observed in Fig. 14 N and shows a difference of  $31.88 \pm 8.22\%$ .

Furthermore, in both Fig. 14 N and O, the structure of single spheroids can be observed (dense cell structures surrounded by no or less cells), which coincides with observations of Fig. 14 L.

Nevertheless, those spheroid structures are not as circular as they were during seeding, showing integration into the tissue formation. This might indicate that a longer culture time is needed for a better spheroid cohesion. Furthermore, the single spheroid structure can mainly be observed in center of the tissue and not in the periphery (yellow arrows), indicating a better spheroid fusion and tissue formation at the outer parts. Nevertheless, as the overall desired tissue fusion occurred for two out of two experiments (tissue formation around five free standing microstructures), the next step is to incorporate cardiomyocytes.

HDF spheroids with a pre-culture of four days (HDF 4)

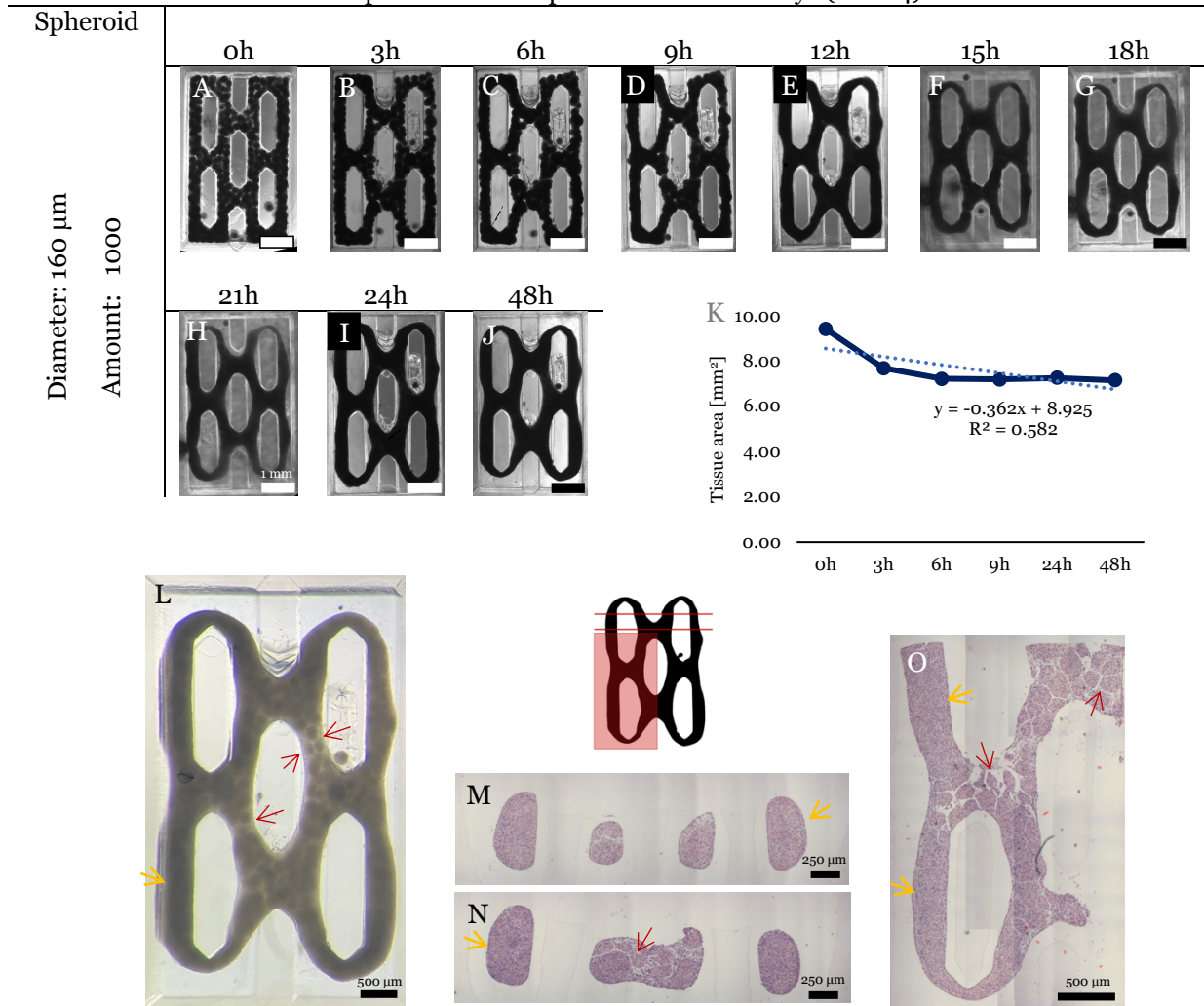


Fig. 14: DIV4 HDF spheroid fusion observed over time (0, 3, 9, 12, 15, 18, 21, 24 and 48h) when seeded in agarose moulds (A to J). Tissue area analysis over time (K), tissue at light overexposure (L), histology of transversal (M and N) and longitudinal (O) cuts after 24h. Two replicates from two independent experiments (one shown in A to F and I to J and tissue area analysis, overexposed image and histology is based on this and one shown in F to H). Unmarked scale bar is 1 mm.

### 4.3. Cardiomyocyte mixed spheroid fusion

In this experiment, rat CMs with HDF mixed spheroids (1:1 ratio) with a pre-culture time of three days (CM-HDF 3) were seeded into the agarose structures (see Fig. 15 A to G). A pre-culture time of three days was chosen since CMs spheroid fusion is slower compared to HDF spheroid fusion, keeping the pre-culture time low to increase the compaction effect of the HDFs [16], [22], [23]. The linear tissue area reduction over time can be seen in Fig. 15 H ( $y = -0.64x + 9.76$ ) with a total decrease of 35.30% after 48h. Also here, the spheroids fused successfully into one single tissue around the microfeatures, with a 11.21% higher tissue area reduction compared to HDF 4 spheroids after 48h (see results section 4.2).

However, the actin filaments (actin, green) and the nuclei (blue) of the CMs and HDFs were stained after 72h and can be seen in Fig. 15 I to R, with Fig. 15 I showing the full tissue size. In Fig. 15 K and Q an anisotropic actin orientation parallel to the pillar length can be observed (see red arrows) [25]. Also, Fig. 15 N shows actin anisotropic orientation in the area that is encapsulated by two microfeatures (see purple arrow). Furthermore, Fig. 15 N also shows isotropic cell orientation in the area that is in contact with three or more pillars (yellow arrow).

Additionally, a difference in fluorescence intensity can be seen for both, the nuclei and the actin, when comparing the tissue in the periphery (Fig. 15 J to L and P to R, higher fluorescent intensity) vs the center (Fig. 15 M to O, lower fluorescent intensity). Also, a higher nuclei signaling amount can be observed in the tissue periphery. As a result, cardiac tissue fusion within the microfeatures, was successful, showing cell alignment in specific tissue regions, indicating a relationship between the microfeatures as structural barriers and cell orientation.

Mix spheroids, rat CMs and HDF (1:1 ratio) with a pre-culture of three days (CM-HDF 3)

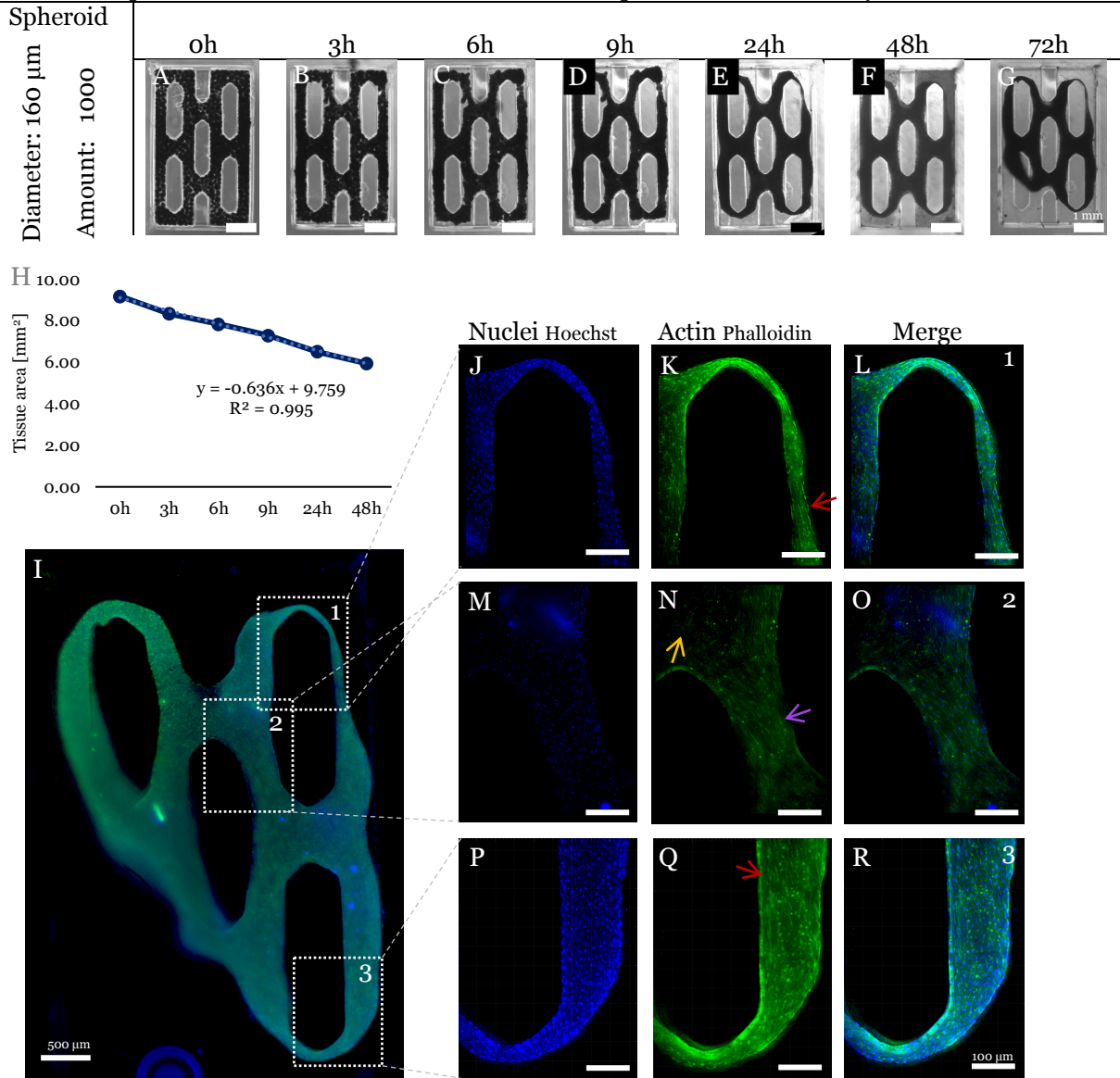


Fig. 15. Rat CMs with HDF mix spheroid (1:1 ratio) with a pre-culture time of three day: spheroid fusion over time (0, 3, 6, 9, 24, 48h) (Unmarked scale bar is 1 mm) (A to G) and the tissue area analysis (H). Fluorescent labeling of the nuclei (blue) and the actin (green) of tissue fusion after 72h (Unmarked scale bar is 100  $\mu\text{m}$ ) (I to R). One replicate from one independent



## Discussion

In this study, the aim was to fabricate a system to control cardiac tissue self-assembly using spheroids as building blocks. An SLA printer was used to design and develop positive resin moulds and to cast negative agarose moulds for cell culture applications. Therefore, troubleshooting and optimization was conducted for the print fidelity, the agarose casting, the spheroid seeding and tissue fusion. As a result, a cardiac tissue was formed and controlled by microfeatures, showing regions of cell alignment and spheroid coherence.

### *Mould design and development*

The first step was to design and develop microfeatures that guide spheroid fusion. A paper and a protocol of Bian et al. [3], [25] was used as a base, as the study explored the anisotropy of engineered cardiac tissue, varying the size, spacing and elongation of elliptical pillars. It was found that the longer the elliptical pillars the greater the tissue alignment, increasing the spreading of the action potential and isometric twitching forces.

Bian et al. used soft lithography to produce PDMS moulds and seeded cells. In contrast, this study utilized an SLA printer, agarose, and spheroids. Attempts to use PDMS casting were made but resulted in poorly defined, uncured structures, as PDMS fails to cure when in contact with the photorein (B). Agarose on the other hand created sharp and defined hole structures (see Fig. 16 C).

To create agarose pillars, a resin mould with elliptical holes was designed (see Fig. 16 D). The holes had a 1:3 elliptical ratio, with lengths ranging from 0.5 mm to 3.0 mm and depths from 0.5 mm to 2 mm. Well-defined agarose pillars were successfully cast only from holes with a depth of 0.5 mm. Deeper holes trapped air bubbles between the resin and agarose, resulting in incomplete or defective pillars (see Fig. 16 E).

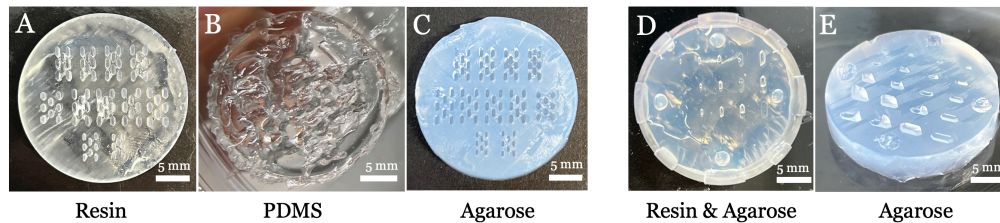


Fig. 16: Casting PDMS (B) and agarose (C) on resin mould (A). Mould including agarose pouring varying hole dimensions (1:3 elliptical pillars, with ranging length of 0.5 to 3.0 mm and depth of 0.5 to 2 mm) (D). Casted agarose from resin mould D (E).

To create sterile agarose moulds, resin moulds were autoclaved in a wet cycle, resulting in fractures and cracks, making the mould not usable (see Fig. 17 A). However, autoclaving it in a dry cycle, the mould had no fractures nor cracks (see results section 1.6).

Since the resin form effects the curing of PDMS, it is essential to test whether the fabricated agarose moulds can be used in cell culture conditions, not harming or influencing the cells behavior. As a proof of concept, agarose moulds were cast from both commercially available silicone moulds (MTPD®) and self-designed moulds. Spheroid fusion after 24 hours was observed in both cases and similar results were achieved for circularity and fusion levels. This indicates that the self-designed agarose moulds are sterile and resistant to cell culture conditions while not influencing the cells behavior (see results section 3).

The next step was to design and develop microfeature moulds, using the photorein manufacture print settings, which resulted in bad fidelity (Fig. 17 B to D).

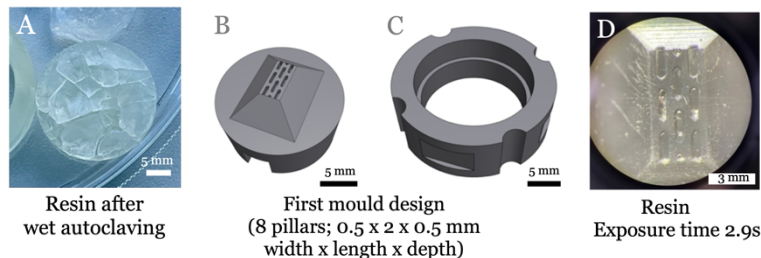


Fig. 17: Resin mould after wet autoclaving (A). First mould design including microfeature (width: 0.5 mm, length: 2 mm and depth 0.5 mm) base (B) and ring (C). Microfeatures after print, wash, and UV curing (exposure time 2.9s, hole width 0.5 mm, length 2 mm and 0.5 mm depth) (D).

To increase the microfeature mould fidelity, a resin mould was designed to explore different print settings like UV light exposure time, layer thickness and print angle (see results section 1.2 and Fig. 18 A and B). The best results were achieved when decreasing the exposure time (from 2.9s to 2.2s), the layer thickness (from 50  $\mu\text{m}$  to 20  $\mu\text{m}$ ) and the print angle to  $0^\circ$  (horizontal), see results section 1.2, Fig. 6. With this experiment, it was found: Decreasing the exposure time increases the overall print fidelity. This was also proven by Wang et al. [45], [46] as it was found: increasing the light duration causes decreased accuracy. Interestingly, Kowsari et al. [45], [47] found, the width and height of the cured print layers increased less linearly with increasing exposure time. In this study, the same was observed for the width (see results section 1.2 and 1.4) but the opposite was observed for the height: cured print layer heights increased less linearly with decreasing exposure time (see results section 1.2). Important to mention is, that for small feature holes, the effect of the exposure time on width influences the height, as at higher exposure times, the hole area gets smaller, closing the hole and thereby decreasing the hole depth (see results section 1.4). Additionally, Kowsari et al. [45], [47] analyzed exposure times of 0.5 to 3s, while in this study exposure times of 1.4 to 2.2s were analyzed, causing the need for more data to compare.

To optimize the print resolution even more, the resin cleaning process was improved by introducing an extra step involving isopropanol sonication (see Fig. 18 C and D). When, using the optimized setting for a microfeature mould with a hole depth of 0.5 mm, then it resulted in a good fidelity (see results section 1.4). However, when printing a mould with an increased hole depth of 1 mm, then the fidelity decreased, which was expected due to the outcome of the previous experiment, creating the need to further decrease the exposure time (1s).

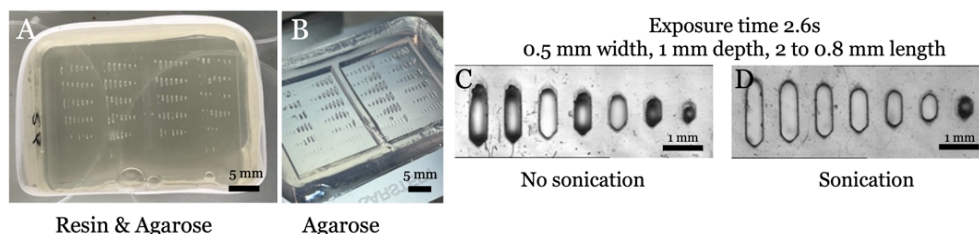


Fig. 18: Resin mould to explore SLA print settings filled with agarose (A) and agarose mould after casting (B). Zoom in of the resin mould after print, wash and UV curing (C) and zoom in on the same design region after additional washing step of isopropanol sonication (D) (Exposure time 2.6s - 0.5 mm width, 1 mm depth, 2 to 0.8 mm length).

Agarose moulds were casted onto the first microfeature mould design (see Fig. 17 B), resulting in poor agarose pillar structures (see Fig. 19 A)

In the literature, vacuuming and centrifugation are commonly used for casting materials [48], [49]. Both methods were tested, with centrifugation effectively removing all air bubbles (see Fig. 19 B). In contrast, vacuuming did not remove all air bubbles (see Fig. 19 C). Various pressure conditions and durations were tested and caused air bubbles to rise from the microfeatures but got trapped in the agarose mould. This occurred because the agarose surface had already gelled, leading to optical interference during imaging. Additionally, it was a challenge to establish a sterile fabrication method using vacuuming.

When centrifuging was implemented, other challenges occurred: The prototype included a ring (see Fig. 17 C) that caused agarose leakage when centrifuging. After redesigning the mould, including a cup (see results section 1.3), the mould shifted to the bottom of the 50 mL falcon, which was hard to access and to remove and it would tilt out of position (see Fig. 19 D). To overcome this, a holder was designed (see results section 1.3 and Fig. 19 E).

Another challenge was to create a flat bottom of the agarose mould, as gelation during centrifugation caused a steep bottom profile, with increasing effect at higher rpm (see Fig. 19 F and G). A steep agarose mould bottom is not preferred as it would create a steep seeding area which might influence the homogeneous spheroid distribution and therefore effects the spheroid fusion.

Additionally, the rotational force during centrifugation caused the agarose release from the cup. When centrifuged shortly (15 seconds) and allowed to gel without external force, a concave meniscus formed (see Fig. 19 H). To create a flat agarose mould bottom, the mould was centrifuged at 700 rpm for 15 seconds, followed by the additional agarose pouring after centrifugation (see results section 1.5).

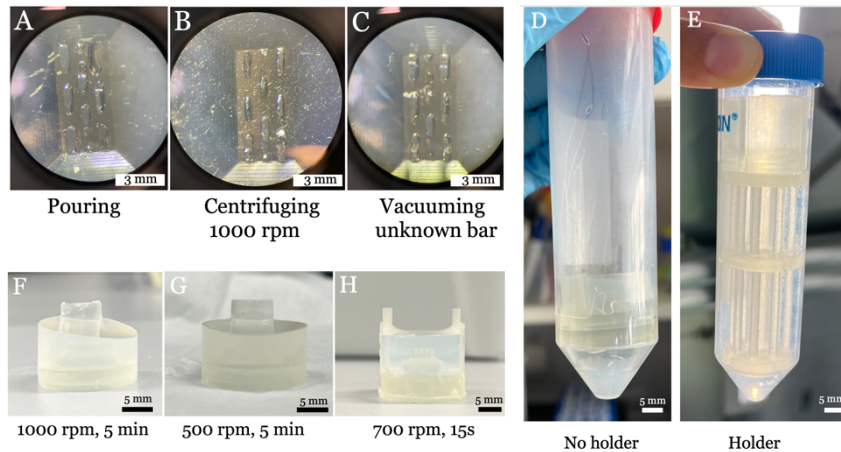


Fig. 19: Agarose mould after casting in first microfeature mould design, when pouring (A), centrifuging at 1000 rpm (B) and vacuuming at unknown bar (C). 50 mL falcon tube including adapted mould (cup) at the bottom (D) and with a designed holder (E). Agarose surface after centrifuging at 1000 rpm for 5 min (F), at 500 rpm for 5 min (G) and at 700 rpm after 15s (H).

As a summary, the microfeature design dimension was compared to the resin and mould microfeatures, resulting in a pillar height of more than 90% for both, the resin and agarose. However, the agarose pillar area was only 78% of the desired structure, creating the need to optimize the resin mould, by designing a larger hole area or decreasing the exposure time even further (see results section 1.6).

Additionally, during the process of releasing the agarose from the resin mould, the microfeatures can break if not handled carefully. Increasing the agarose microfeatures height, increases the risk of breakage. A resin depth of 0.5 mm did not cause any agarose pillar breakage, while a depth of 1 mm did. As a result, the mould release should be optimized by for example including special release features like gaps to better access the interface of resin and agarose mould.

A limitation of the mould fabrication process is upscaling due to centrifugation, as the mould is placed into a 50 mL falcon tube with a diameter of 30 mm. An upscaled version of the seeding area of approximately 50 mm<sup>2</sup> can be seen in Fig. 20 (A technical drawing can be seen in the appendix).

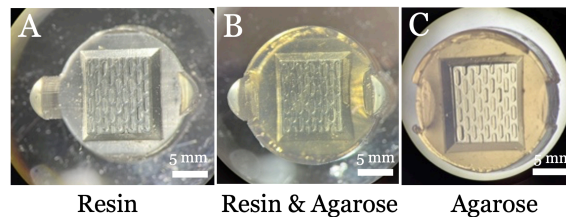


Fig. 20: Upscaling the seeding area to 52.70 mm<sup>2</sup>. Resin after print, wash and UV curing at exposure time 1s (A), resin with agarose casted and gelled (B) and the agarose mould (C).

### Tissue formation

After initial cell experiments of seeding HDF spheroid with a pre-culture time of three days (HDF 3) into an agarose mould with a pillar height of 0.5 mm, the spheroids stacked and collected at the top of the pillars. This prevented the effect of tissue formation around the microfeatures and created the need to increasing the pillar height (see results section 4.1, Fig. 13 A to E). A height of 0.8 and 1 mm was selected for further testing, and the results can be seen in results section 4.1 and Fig. 21. For the pillar height of 1 mm, for the first time, tissue formation occurred around two out of five free standing pillars after 24 hours, selecting this height for further experiments (see Fig. 21 D to F). An optimal tissue formation would be around five out of five free standing pillars (excluding the two pillars that are attached to the wall).

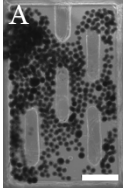
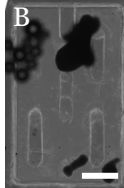
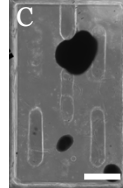
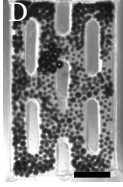
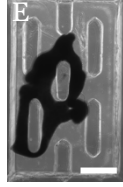
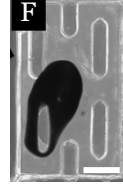
HDF spheroids with a pre-culture of three days (HDF 3)					
Pillar height [mm]	Spheroid		1h	24h	72h
	Diameter [ $\mu\text{m}$ ]	Amount			
0.8	160	400			
1	160	400			

Fig. 21: HDF 3 spheroid seeding in a mould with a pillar height of 0.8 mm at timepoint 1, 24 and 72 hours (A to C). HDF 3 spheroid seeding in a mould with a pillar height of 1 mm at timepoint 1, 24 and 72 hours (D to F). Scale bar is 1 mm.

Following, an experiment was conducted, varying the seeding density and subsequently establishing three key requirements to create uniform tissue formation:

- ◆ **Spheroid seeding concentration:** Determine and optimize the spheroid concentration in media before seeding.
- ◆ **Homogeneous spheroid distribution:** Distribute spheroids evenly within the moulds seeding area.
- ◆ **Vertical spheroid stacking:** Seed more than one layer of spheroids to avoid gap formation.

However, seeding HDF 3 did not form the desired tissue formation, as the tissue either formed gaps or lifts off the microstructures after 24 hours (see results section 4.1, Fig. 14 E, Q, W). Interestingly, Dean et al. [13] studied the normal human fibroblast (NHF) self-assembly, seeding cells into a honeycombs structure and found, within 12 to 15 hours the tissue generated enough radial tension to lift off the mould. This seems also to be the case in this study for HDF 3 at a higher spheroid seeding density or lower agarose pillar height (see results section 4.1, Fig. 14 E and W). This experiment also indicates tissue radial tension generation, as the tissue area decreased mainly in the periphery of the tissue within 9 hours. Additionally, the tissue created a spheroid structure after 48 hours, which is the minimal surface energy and area. Also, NHF tissue lift off was controlled by Svoronos et al. [50], as the effect of changing the mould design onto the tissue self-organization was investigated. A honeycomb shape with post and cone shaped pillars was used, resulting in tissue detachment of the cone pillars quicker compared to the post pillars. However, after 24 hours, the tissue fully detached from the mould.

In this study, the spheroid pre-culture time was increased from three to four days (HDF 4), resulting in the desired tissue formation, indicating a lower radial force for HDF 4 compared to HDF 3. The HDF 4 tissue showed smooth edges after 48 hours. Matching to this, Rago et al. [23] used NHF spheroids with a pre-culture time of one day and seeded them into a ring and honeycomb shape (pillars: 600  $\mu\text{m}$  in diameter and 700  $\mu\text{m}$  depth). The spheroids compacted to a single tissue around the pillars showing smooth edges after 24 hours and the tissue did not lift off the mould. Vrij et al. [20], studied the effect of directing spheroid fusion by changing complex mould shapes and found that the largest tissue displacement appeared in the corners of the mould. This can also be observed in this study (see results section 4.2, Fig. 14 E to J).

Rago et al. [23] also studied the spheroid fusion behavior when varying the pre-culture time (1, 4 and 7 days) of NHF spheroids and found that a longer pre-culture time results in a slower spheroid fusion, a lower spheroid coherence and a closer tissue structure to its initial formation. In this study, when comparing the first 9 hours of the tissue compaction of HDF 3 ( $0.206 \frac{\text{mm}^2}{\text{h}}$ ) vs HDF 4 ( $0.247 \frac{\text{mm}^2}{\text{h}}$ ), it can be seen that the area reduction of HDF 4 is  $0.041 \frac{\text{mm}^2}{\text{h}}$  faster. Only the first 9 hours are incorporated, as for HDF 3 the tissue lifts off the microfeatures afterwards, making it not comparable. This outcome wouldn't be expected when comparing it to the mentioned paper. However, the outcome is based on single experiments and the spheroid and aggregate size (amount of spheroids seeded) was different for HDF 3 and HDF 4, which can influence the fusion behavior (HDF 3: 900 spheroids, 175  $\mu\text{m}$  diameter and HDF 4: 1000 spheroids, 160  $\mu\text{m}$  diameter, see results section 4.1 and 4.2). For all tissue area measurements, the error of the segmentation is unknown. Nevertheless, the error is the same for the analysis, making a comparison still possible.

To prevent the tissue lift off, implementing T-shaped pillars or a lid (like lab-on-chip) might be an option to explore. However, Vrij et al. [20], studied the difference of using cells and spheroids as building blocks and found, spheroid contraction occurs in a controlled way while cells compact too strong and thereby losing the initial tissue structure. This coincides with the outcome of the previous papers and indicates the importance of using spheroids instead of cells as building blocks.

Additionally, single spheroids can be observed on top of the pillars in the results section 4.2. This might be prevented, when designing triangular roof pillars, to let the spheroid slide into the seeding area.

As a desired tissue fusion occurred using HDF 4 spheroids, implementing CMs was the next step. Literature indicates [16], [22], [23], that the spheroid fusion of CMs only is slower compared to fibroblast spheroids. Therefore, human CM spheroids were seeded and their fusion behavior (tissue area reduction over time) was analyzed resulting in fusion speed of  $0.013 \frac{\text{mm}^2}{\text{h}}$  within the first 9 hours. As this is only 5.34% of the fusion speed of HDF 4 (see results section 4.2), it coincides with the findings of the previously mentioned papers (see appendix section 3). In order to cause tissue fusion using CMs, the mentioned papers [16], [22], [23] show that incorporating fibroblasts creates a structurally supportive environment that promotes tissue remodeling, improves cell-cell communication, and enhances the maturation of hiPSC-CMs.

Therefore, mixed cell spheroids including rat CMs and HDF (1:1 ratio), were seeded with a pre-culture time of three days (CM-HDF 3). Three days was chosen based on the spheroid shape (compaction and circularity) and based on literature, since CM spheroids fuse slower compared to HDF spheroids, keeping the pre-culture time low to increase the compaction effect of the HDFs. The CM-HDF 3 fusion resulted in the desired tissue shape of a single tissue wrapped around the five free standing microfeatures (see result section 4.3). Unfortunately, the image at 24 hours of CM-HDF 3 (see results section 4.3, Fig. 15 F) indicates a bacterial contamination. To create a higher tissue to mould contrast during imaging, the tissue was flushed with media, releasing the left corner of the tissue from the mould.

The rat CMs provider stated that cells will spontaneously contract after 24 hours of culture. However, in this study, no contraction was observed. This might be due to the extended two-week cell culture before creating spheroid. Increasing the cell culture duration, increases cell morphological changes which might reduce the chances of cell beating. [6], [7], [10]

The overexposed image and histology (spheroid coherence) of the HDF 4 and the actin staining (cell alignment) of the CM-HDF 3 can be used to analyze the relationship between structural barriers and cellular forces.

The heterogenic cell density can be checked by the nuclei staining of the CM-HDF 3. All tissue regions in the periphery have an increased cell amount compared to the center of the tissue (see fluorescent intensity and signaling amount of Fig. 15 L, O and R, results section 4.3). This is not only the case for the CM-HDF 3 but is also for the HDF 4 tissue, as the transversal cuts show an increase in tissue thickness in the periphery (see results section 4.2, Fig. 14 N). Additionally, this coincides with the over exposed image where darker regions in the outer area indicates a higher cell density compared to the center. This was also found in the previously mentioned study by Vrij et al. [20] as it was noticed, that the tissue compaction led to a heterogenic cell density, with a higher density in the periphery compared to the center.

Next, the cell orientation can be observed through the actin staining of CM-HDF 3, showing anisotropic orientation in the periphery of the tissue parallel to the pillar length and in the center when encapsulated by two microfeatures (see results section 4.3, Fig. 15 K and Q, red arrows). Regions that are in contact with three or four microfeatures show an isotropic cell orientation (see results section 4.3, Fig. 15 N, yellow arrows). A simplified visualization of the isotropic regions can be seen in Fig. 22 highlighted in red. When comparing this outcome to the histology of HDF 4, then we can see that tissue regions that are in contact with three or more microfeature show a decrease in spheroid coherence (see results section 4.2, Fig. 14 O, Fig. 22, highlighted in red). This is also schematically visualized by Fig. 22 highlighted in red. These findings indicate a relationship between cell orientation and spheroid coherence, but more data is needed as the findings are based on different cell types (HDF 4 and CM-HDF 3).

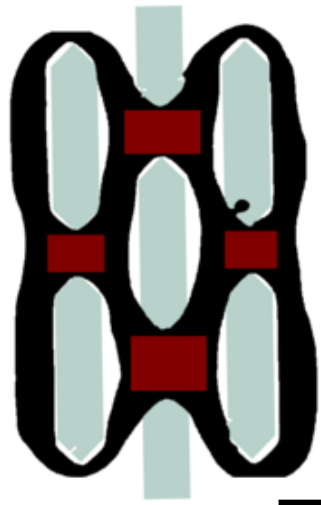


*Fig. 22: A schematic visualization of CM-HDF 3 with isotropic cell orientation regions marked in red and anisotropic regions in black after 72 hours. At the same time, a schematic visualization of HDF 4 after 48 hours with reduced spheroid coherence marked in red and areas of increased tissue coherence marked in black. Scale bar 1 mm.*

To summarize, it was found that reducing the SLA exposure time (1s) and print angle ( $0^\circ$ ) increases the design fidelity. Also, to create homogeneous tissue formation three key requirements were established:

(i) Determining the spheroid seeding concentration prior seeding, (ii) create homogeneous spheroid distribution and (iii) vertical spheroid stacking. Additionally, the tissue fusion speed is depended on the cell type(s) with HCMs being the slowest and HDF 3 the fastest, when comparing HDF 3, HDF 4, CM-HDF 3 and HCM 3. Also increasing the HDF spheroid pre-culture time of three to four days reduced radial tissue forces and resulted in no tissue release from the microfeatures. HDF 4 spheroid fusion showed increased spheroid coherence and cell density in the tissue periphery. CM-HDF 3 also demonstrated a higher cell density in the outer tissue areas and also an anisotropic cell orientation. Isotropic cell orientation on the other hand, was observed in the areas surrounded by three or four microfeatures. The results indicate a relationship between spheroid coherence and cell alignment to structural barriers.

## Outlook

In the following, future steps are listed that either (1) support or (2) extend the study's aim.

### 1. Steps to support the study's aim

Further steps can be taken to confirm the achievement of the study's aim:

- (i) To further analyze the cell orientation, a software such as Imaris can be used. Therefore, precise tension areas within the mould could be determined and used to study designs with increased cell alignment. One example is the paper of Schell et al. [34], studying the control of cell ECM synthesis by varying mould designs. Therefore, a software was used to predict regions of cell alignment.
- (ii) A cell viability and cytotoxicity assays should be implemented to check if the tissue has a necrotic core. Even though, for example the tissue thickness of HDF 4 is only a few hundred micrometers after 48 hours, the tissue thickness at timepoint zero is unknown and might restrict oxygen and nutrition diffusion to the core.
- (iii) The sterile agarose mould fabrication can be simplified by producing non-sterile moulds and sterilizing them using ethanol. This was tested using HDF 4 but resulted in reduced spheroid fusion speed (see appendix section 2). However, this experiment should be repeated with increasing equilibration steps and duration, to ensure the ethanol removal from the agarose moulds.

### 2. Steps to extend the study's aim

To better understand the relationship between mould structure and tissue function, and to develop cardiac tissue that closely mimics the *in vivo* conditions for potential cell-based therapy, several steps can be conducted:

- (i) By exploring the design of the microfeatures (size, shape, pillar-to-pillar distance), to increase the ratio of aligned to unaligned cell areas, to increase tissue functionality. [3], [4], [5], [6]
- (ii) Explore the relationship between tissue tension, spheroid coherence and cell alignment by performing, histology and actin filament staining at the same cell and culture conditions.
- (iii) In general, microfeatures and spheroid size ratios can be changed and analyzed. Therefore, smaller spheroid sizes can be explored to seed two or more spheroid layer, while staying in the limiting diffusion radius.
- (iv) Mould upscaling is needed to create a meaningful impact *in vivo*. [8], [11]
- (v) Vascularized spheroids could be used to further upscale the 3D cardiac tissue: There is preliminary study on spheroid vascularization increasing the possibility for using pre-vascularized spheroids as building blocks, counteracting the limiting diffusion radius of oxygen and nutrition's. [51]
- (vi) Including spontaneously contracting CMs to explore contraction, forces and the propagation of electrical signals as well as cell maturation. Therefore, analyzing tools like impedance spectroscopy, sharp microelectrode pipettes and multi-electrode arrays can be implemented into the mould or CMs can be stained with calcium-binding fluorescent and voltage-sensitive dyes. [10]
- (vii) To create a more *in vivo* like cardiac tissue, cell types like endothelial cells, pericytes and fibroblasts can be implemented. The cell types can be fluorescently labeled differently in order to investigate self-assembly.

## Conclusion

This study successfully developed a system to control cardiac tissue self-assembly using spheroids as building blocks. Positive resin moulds were fabricated using an SLA printer and negative agarose moulds were casted using centrifugation. Reducing the SLA exposure time to 1s and the print angle to 0° improved resin fidelity. Centrifugation of 700 rpm for 15s was implemented to cast agarose moulds including high-resolution microfeatures that guided HDF and rat CM-HDF spheroid fusion. HDF spheroids were used to explore the spheroid pre-culture time and seeding density to create successful tissue fusion after 48 hours and three key requirements for homogeneous tissue formation were established: (i) Determining the spheroid seeding concentration prior seeding, (ii) create homogeneous spheroid distribution and (iii) vertical spheroid stacking. HDF spheroids with a pre-culture time of four days, a diameter of 160 µm and a density of 1000 spheroid per 10.67 mm<sup>2</sup> were used and resulted in a tissue thickness ranging from 65 µm to 117 µm. Both, HDF and rat CM-HDF resulted in successful tissue formation with a heterogeneous cellular density observed by an overexposed image, histology (HDF) and nuclei staining (CM-HDF). Therefore, cell density was higher in the tissue periphery compared to the center. Additionally, heterogeneous cell orientation was observed by staining the cells actin filament. Cells located in the periphery had an anisotropic orientation, while an isotropic orientation was observed in regions surrounded by three or four microfeatures. These findings indicate a relationship between spheroid coherence and cell alignment to structural barriers.

## Acknowledgment

First, I would like to thank Jun.-Prof. Dr.-Ing. Daniela Duarte Campos, Dr. Oscar O'Dwyer Lancaster-Jones, and Dr.-Ing. Jeroen Rouwkema for enabling the collaboration between the University of Twente and Ruprecht-Karls-Universität Heidelberg, which allowed me to write my thesis abroad. This experience has been an important step in my academic development, so thank you Jun.-Prof. Dr.-Ing. Daniela Duarte Campos for hosting me in your lab.

I am especially grateful to Dr. Oscar O'Dwyer Lancaster-Jones for his supervision and guidance throughout my project. Your support and patience were invaluable, and I hope the plants in our office continue to thrive.

Thank you to Meng Wang for her assistance and for taking care of some of my cells and spheroids. I am also grateful to Kilian Paul for helping analyze spheroid fusion behavior, as well as to Dr. Verena Schwach and Dr. Vasileios Trikalitis for their guidance and for sharing their expertise. It was a pleasure working with you, as well as with Andrea Frank and Dr. Russell Louis Quinn. Thank you for your advice and help when I needed it.

Overall, I would like to thank the Duarte Campos group for welcoming me so kindly. Special thanks to Alexandre Georges Taoum for your music during lab work, to Ole Max Niklas Thaden for keeping me company during late office hours, to Mario Wisbar for being a great desk neighbor, and to Erin Spiller for our great conversations.

Finally, I want to thank my family and friends for their ongoing encouragement and support.



## References

- [1] P. Montero *et al.*, “Cells, Materials, and Fabrication Processes for Cardiac Tissue Engineering,” 2020. doi: 10.3389/fbioe.2020.00955.
- [2] R. Langer and J. Vacanti, “Advances in tissue engineering,” in *Journal of Pediatric Surgery*, 2016. doi: 10.1016/j.jpedsurg.2015.10.022.
- [3] W. Bian, B. Liao, N. Badie, and N. Bursac, “Mesoscopic hydrogel molding to control the 3d geometry of bioartificial muscle tissues,” *Nat Protoc*, vol. 4, no. 10, 2009, doi: 10.1038/nprot.2009.155.
- [4] L. He and X. Chen, “Cardiomyocyte Induction and Regeneration for Myocardial Infarction Treatment: Cell Sources and Administration Strategies,” 2020. doi: 10.1002/adhm.202001175.
- [5] B. Orsolits, Z. Kovács, J. Kriston-Vizi, B. Merkely, and G. Földes, “New Modalities of 3D Pluripotent Stem Cell-Based Assays in Cardiovascular Toxicity,” 2021. doi: 10.3389/fphar.2021.603016.
- [6] M. F. Tenreiro, A. F. Louro, P. M. Alves, and M. Serra, “Next generation of heart regenerative therapies: progress and promise of cardiac tissue engineering,” 2021. doi: 10.1038/s41536-021-00140-4.
- [7] E. Mohr, T. Thum, and C. Bär, “Accelerating cardiovascular research: recent advances in translational 2D and 3D heart models,” 2022. doi: 10.1002/ejhf.2631.
- [8] W. H. Zimmermann and R. Cesnjevar, “Cardiac tissue engineering: Implications for pediatric heart surgery,” in *Pediatric Cardiology*, 2009. doi: 10.1007/s00246-009-9405-6.
- [9] W. H. Zimmermann *et al.*, “Heart muscle engineering: An update on cardiac muscle replacement therapy,” 2006. doi: 10.1016/j.cardiores.2006.03.023.
- [10] C. Zuppinger, “3D Cardiac Cell Culture: A Critical Review of Current Technologies and Applications,” 2019. doi: 10.3389/fcvm.2019.00087.
- [11] T. Rademakers, J. M. Horvath, C. A. van Blitterswijk, and V. L. S. LaPointe, “Oxygen and nutrient delivery in tissue engineering: Approaches to graft vascularization,” 2019. doi: 10.1002/term.2932.
- [12] E. Fennema, N. Rivron, J. Rouwkema, C. van Blitterswijk, and J. De Boer, “Spheroid culture as a tool for creating 3D complex tissues,” 2013. doi: 10.1016/j.tibtech.2012.12.003.
- [13] D. M. Dean, A. P. Napolitano, J. Youssef, and J. R. Morgan, “Rods, tori, and honeycombs: the directed self-assembly of microtissues with prescribed microscale geometries,” *The FASEB Journal*, vol. 21, no. 14, 2007, doi: 10.1096/fj.07-8710com.
- [14] M. Schot, N. Araújo-Gomes, B. van Loo, T. Kamperman, and J. Leijten, “Scalable fabrication, compartmentalization and applications of living microtissues,” *Bioact Mater*, vol. 19, 2023, doi: 10.1016/j.bioactmat.2022.04.005.
- [15] D. Liu, S. Chen, and M. Win Naing, “A review of manufacturing capabilities of cell spheroid generation technologies and future development,” 2021. doi: 10.1002/bit.27620.
- [16] R. Noguchi *et al.*, “Development of a three-dimensional pre-vascularized scaffold-free contractile cardiac patch for treating heart disease,” *Journal of Heart and Lung Transplantation*, vol. 35, no. 1, 2016, doi: 10.1016/j.healun.2015.06.001.
- [17] K. L. Wang, Q. Xue, X. H. Xu, F. Hu, and H. Shao, “Recent progress in induced pluripotent stem cell-derived 3D cultures for cardiac regeneration,” 2021. doi: 10.1007/s00441-021-03414-x.
- [18] D. Banerjee *et al.*, “Strategies for 3D bioprinting of spheroids: A comprehensive review,” 2022. doi: 10.1016/j.biomaterials.2022.121881.
- [19] P. Zhuang, Y. H. Chiang, M. S. Fernanda, and M. He, “Using Spheroids as Building Blocks Towards 3D Bioprinting of Tumor Microenvironment,” 2021. doi: 10.18063/IJB.V7I4.444.
- [20] E. Vrij, J. Rouwkema, V. Lapointe, C. Van Blitterswijk, R. Truckenmüller, and N. Rivron, “Directed Assembly and Development of Material-Free Tissues with Complex Architectures,” *Advanced Materials*, vol. 28, no. 21, 2016, doi: 10.1002/adma.201505723.
- [21] B. R. Desroches *et al.*, “Functional scaffold-free 3-D cardiac microtissues: A novel model for the investigation of heart cells,” *Am J Physiol Heart Circ Physiol*, vol. 302, no. 10, 2012, doi: 10.1152/ajpheart.00743.2011.
- [22] T. Y. Kim *et al.*, “Directed fusion of cardiac spheroids into larger heterocellular microtissues enables investigation of cardiac action potential propagation via cardiac fibroblasts,” *PLoS One*, vol. 13, no. 5, 2018, doi: 10.1371/journal.pone.0196714.
- [23] A. P. Rago, D. M. Dean, and J. R. Morgan, “Controlling cell position in complex heterotypic 3D microtissues by tissue fusion,” *Biotechnol Bioeng*, vol. 102, no. 4, 2009, doi: 10.1002/bit.22162.

- [24] K. Jakab *et al.*, “Tissue engineering by self-assembly of cells printed into topologically defined structures,” *Tissue Eng Part A*, vol. 14, no. 3, 2008, doi: 10.1089/tea.2007.0173.
- [25] W. Bian, C. P. Jackman, and N. Bursac, “Controlling the structural and functional anisotropy of engineered cardiac tissues,” *Biofabrication*, vol. 6, no. 2, 2014, doi: 10.1088/1758-5082/6/2/024109.
- [26] F. Weinberger, I. Mannhardt, and T. Eschenhagen, “Engineering Cardiac Muscle Tissue: A Maturing Field of Research,” 2017. doi: 10.1161/CIRCRESAHA.117.310738.
- [27] E. Querdel *et al.*, “Human Engineered Heart Tissue Patches Remuscularize the Injured Heart in a Dose-Dependent Manner,” *Circulation*, vol. 143, no. 20, 2021, doi: 10.1161/CIRCULATIONAHA.120.047904.
- [28] J. Veldhuizen, J. Cutts, D. A. Brafman, R. Q. Migrino, and M. Nikkhah, “Engineering anisotropic human stem cell-derived three-dimensional cardiac tissue on-a-chip,” *Biomaterials*, vol. 256, 2020, doi: 10.1016/j.biomaterials.2020.120195.
- [29] M. Tiburcy *et al.*, “Defined engineered human myocardium with advanced maturation for applications in heart failure modeling and repair,” *Circulation*, vol. 135, no. 19, 2017, doi: 10.1161/CIRCULATIONAHA.116.024145.
- [30] D. Zhang, I. Y. Shadrin, J. Lam, H. Q. Xian, H. R. Snodgrass, and N. Bursac, “Tissue-engineered cardiac patch for advanced functional maturation of human ESC-derived cardiomyocytes,” *Biomaterials*, vol. 34, no. 23, 2013, doi: 10.1016/j.biomaterials.2013.04.026.
- [31] W. Bian, N. Badie, H. D. Himel, and N. Bursac, “Robust T-tubulation and maturation of cardiomyocytes using tissue-engineered epicardial mimetics,” *Biomaterials*, vol. 35, no. 12, 2014, doi: 10.1016/j.biomaterials.2014.01.045.
- [32] B. Liao, N. Christoforou, K. W. Leong, and N. Bursac, “Pluripotent stem cell-derived cardiac tissue patch with advanced structure and function,” *Biomaterials*, vol. 32, no. 35, 2011, doi: 10.1016/j.biomaterials.2011.08.050.
- [33] W. Bian, M. Juhas, T. W. Pfeiler, and N. Bursac, “Local tissue geometry determines contractile force generation of engineered muscle networks,” *Tissue Eng Part A*, vol. 18, no. 9–10, 2012, doi: 10.1089/ten.tea.2011.0313.
- [34] J. Y. Schell *et al.*, “Harnessing cellular-derived forces in self-assembled microtissues to control the synthesis and alignment of ECM,” *Biomaterials*, vol. 77, 2016, doi: 10.1016/j.biomaterials.2015.10.080.
- [35] P. Bose, J. Eyckmans, T. D. Nguyen, C. S. Chen, and D. H. Reich, “Effects of Geometry on the Mechanics and Alignment of Three-Dimensional Engineered Microtissues,” *ACS Biomater Sci Eng*, vol. 5, no. 8, 2019, doi: 10.1021/acsbomaterials.8b01183.
- [36] W. R. Legant, A. Pathak, M. T. Yang, V. S. Deshpande, R. M. McMeeking, and C. S. Chen, “Microfabricated tissue gauges to measure and manipulate forces from 3D microtissues,” *Proc Natl Acad Sci U S A*, vol. 106, no. 25, 2009, doi: 10.1073/pnas.0900174106.
- [37] A. Gerami *et al.*, “Microfluidics for Porous Systems: Fabrication, Microscopy and Applications,” *Transp Porous Media*, vol. 130, no. 1, 2019, doi: 10.1007/s11242-018-1202-3.
- [38] C. Wu, R. Yi, Y. J. Liu, Y. He, and C. C. L. Wang, “Delta DLP 3D printing with large size,” in *IEEE International Conference on Intelligent Robots and Systems*, 2016. doi: 10.1109/IROS.2016.7759338.
- [39] A. P. Napolitano *et al.*, “Scaffold-free three-dimensional cell culture utilizing micromolded nonadhesive hydrogels,” *Biotechniques*, vol. 43, no. 4, 2007, doi: 10.2144/000112591.
- [40] P. Zarrintaj *et al.*, “Agarose-based biomaterials for tissue engineering,” 2018. doi: 10.1016/j.carbpol.2018.01.060.
- [41] N. Tanaka *et al.*, “Microcasting with agarose gel: Via degassed polydimethylsiloxane molds for repellency-guided cell patterning,” *RSC Adv*, vol. 6, no. 60, 2016, doi: 10.1039/c6ra11563b.
- [42] BioRender, “Biorender Templates,” BioRender.
- [43] “24-24TR Rods — 3D Petri Dish by Microtissues, Inc.” Accessed: Dec. 06, 2024. [Online]. Available: <https://www.microtissues.com/buy-now/24-24-rods>
- [44] H. Jawad, A. R. Lyon, S. E. Harding, N. N. Ali, and A. R. Boccaccini, “Myocardial tissue engineering,” 2008. doi: 10.1093/bmb/ldno26.
- [45] T. R. Mhmoood and N. K. Al-Karkhi, “A Review of the Stereo lithography 3D Printing Process and the Effect of Parameters on Quality,” *Al-Khwarizmi Engineering Journal*, vol. 19, no. 2, 2023, doi: 10.22153/kej.2023.04.003.

- [46] W. L. Wang, C. M. Cheah, J. Y. H. Fuh, and L. Lu, "Influence of process parameters on stereolithography part shrinkage," *Mater Des*, vol. 17, no. 4, 1996, doi: 10.1016/S0261-3069(97)00008-3.
- [47] K. Kowsari, S. Akbari, D. Wang, N. X. Fang, and Q. Ge, "High-Efficiency High-Resolution Multimaterial Fabrication for Digital Light Processing-Based Three-Dimensional Printing," *3D Print Addit Manuf*, vol. 5, no. 3, 2018, doi: 10.1089/3dp.2018.0004.
- [48] H. A. Strobel, E. L. Calamari, B. Alphonse, T. A. Hookway, and M. W. Rolle, "Fabrication of custom agarose wells for cell seeding and tissue ring self-assembly using 3D-printed molds," *Journal of Visualized Experiments*, vol. 2018, no. 134, 2018, doi: 10.3791/56618.
- [49] S. Gholami, M. M. Mohebi, E. Hajizadeh-Saffar, M. H. Ghanian, I. Zarkesh, and H. Baharvand, "Fabrication of microporous inorganic microneedles by centrifugal casting method for transdermal extraction and delivery," *Int J Pharm*, vol. 558, 2019, doi: 10.1016/j.ijpharm.2018.12.089.
- [50] A. A. Svoronos, N. Tejavibulya, J. Y. Schell, V. B. Shenoy, and J. R. Morgan, "Micro-mold design controls the 3d morphological evolution of self-assembling multicellular microtissues," *Tissue Eng Part A*, vol. 20, no. 7–8, 2014, doi: 10.1089/ten.tea.2013.0297.
- [51] U. Arslan *et al.*, "Vascularized hiPSC-derived 3D cardiac microtissue on chip," *Stem Cell Reports*, vol. 18, no. 7, 2023, doi: 10.1016/j.stemcr.2023.06.001.

# Appendix

In the following, technical drawings of the mould, an upscaled version of the mould, as well as the holder are shown. Additionally, two spheroid seeding experiments are presented: sterilizing agarose moulds with ethanol seeding HDF 4 and producing agarose mould in the established way (see method section 1.3) seeding spheroid primary human CMs.

## 1. Technical drawings of the mould designs

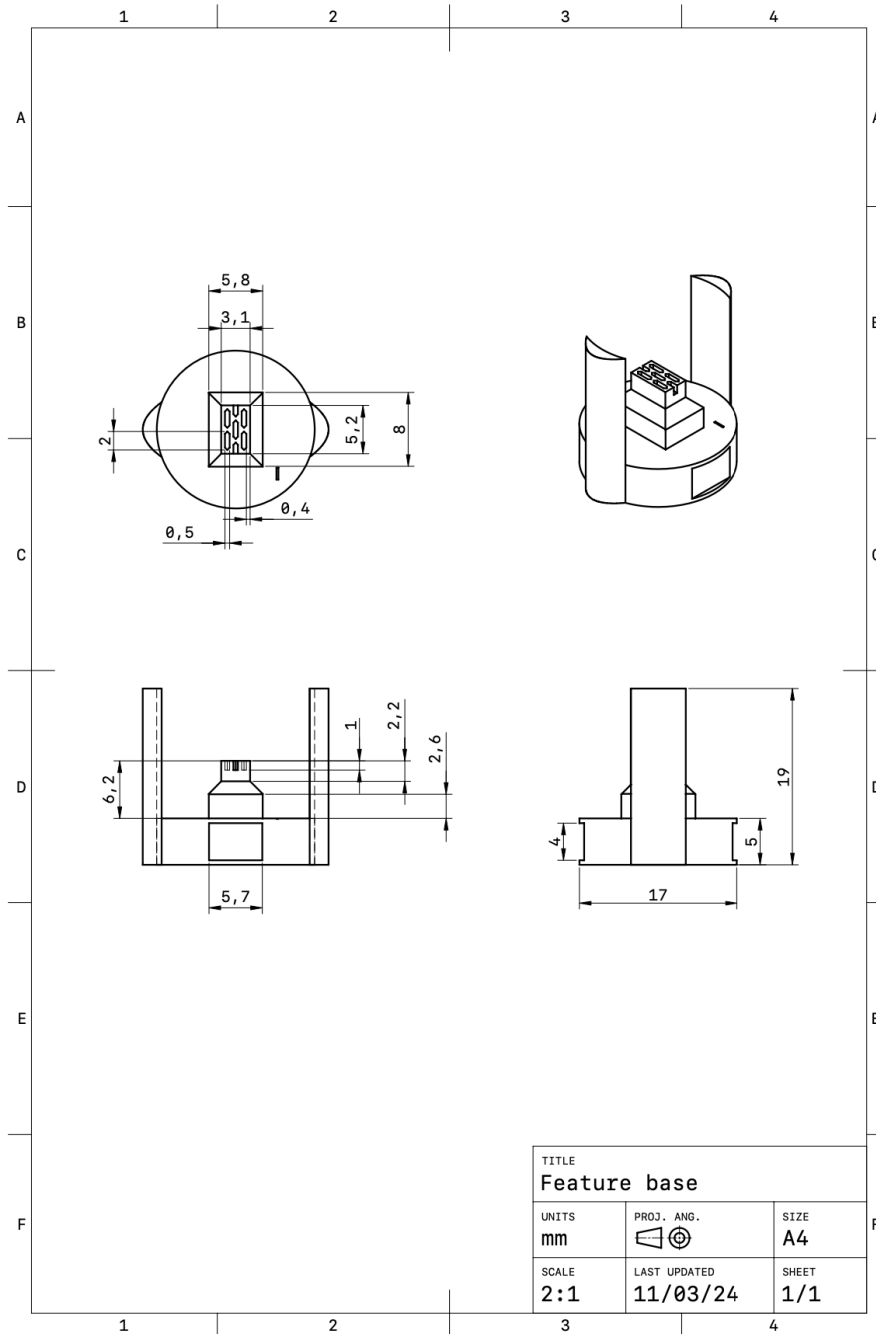


Fig. 23: Technical drawing of the feature base with a seeding area of 10.67 mm<sup>2</sup>.

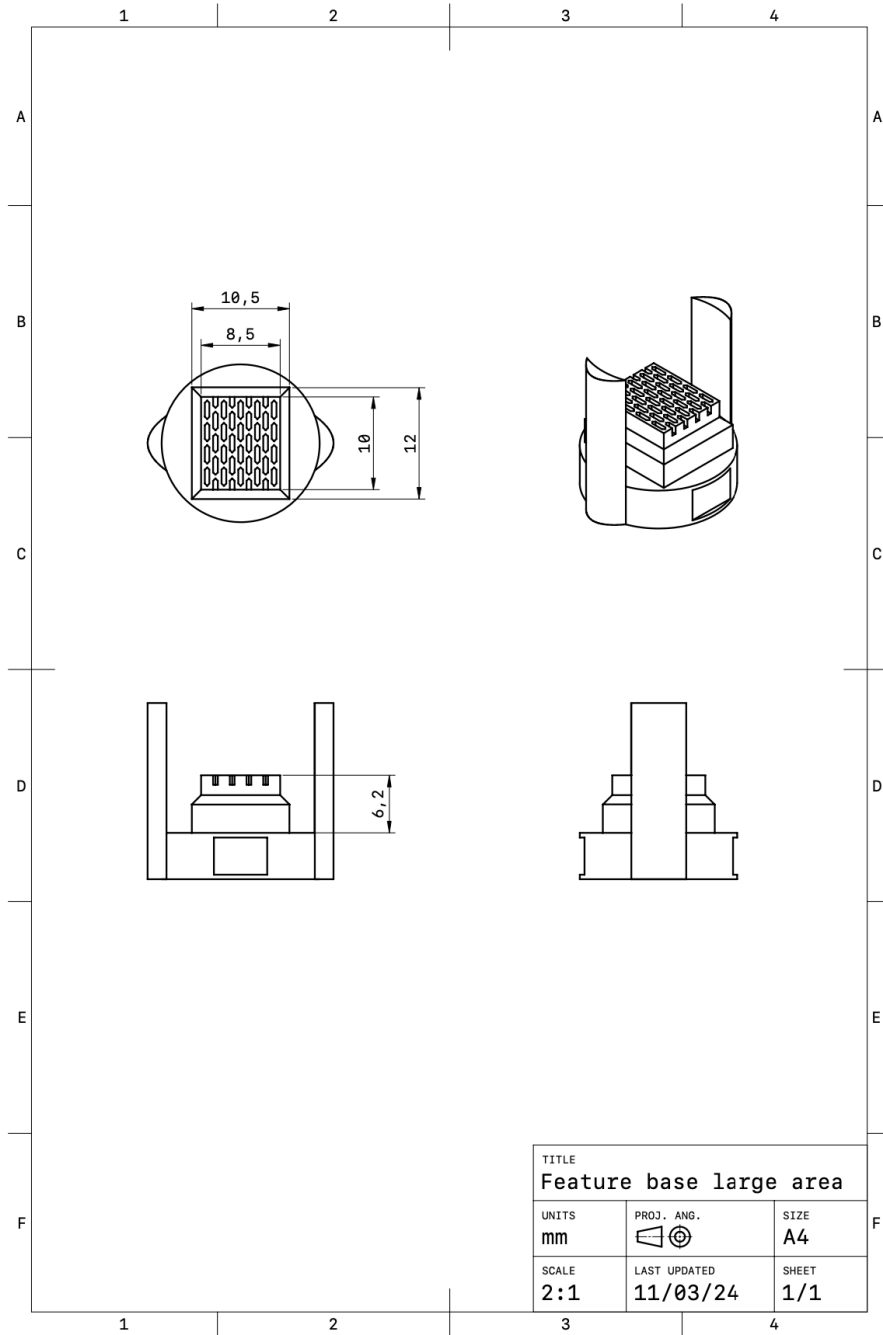


Fig. 24: Technical drawing of the upscaled feature base with a seeding area of 52.70 mm<sup>2</sup>. Further mould details can be seen in Fig. 23.

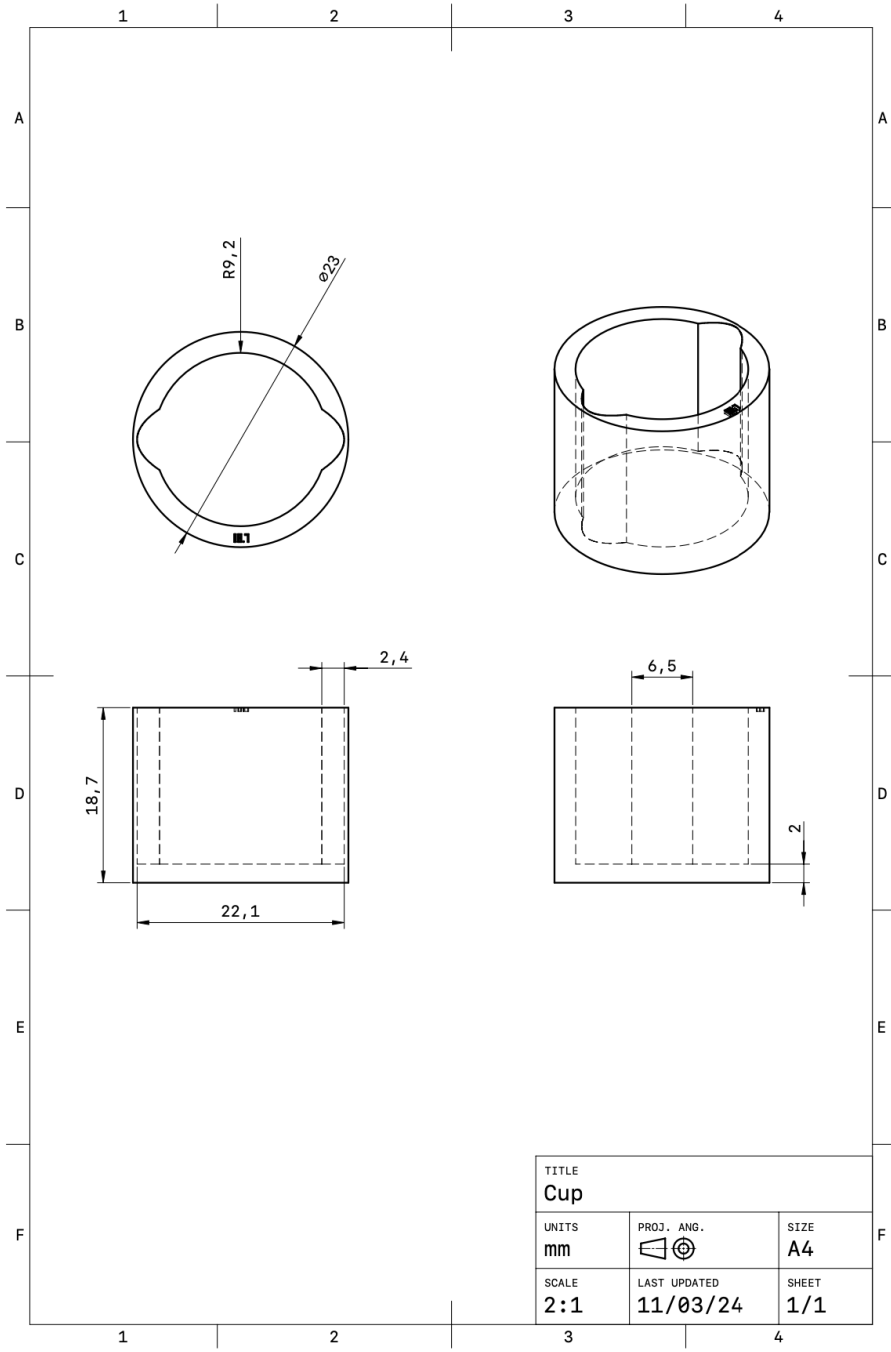


Fig. 25: Technical drawing of the mould cup.

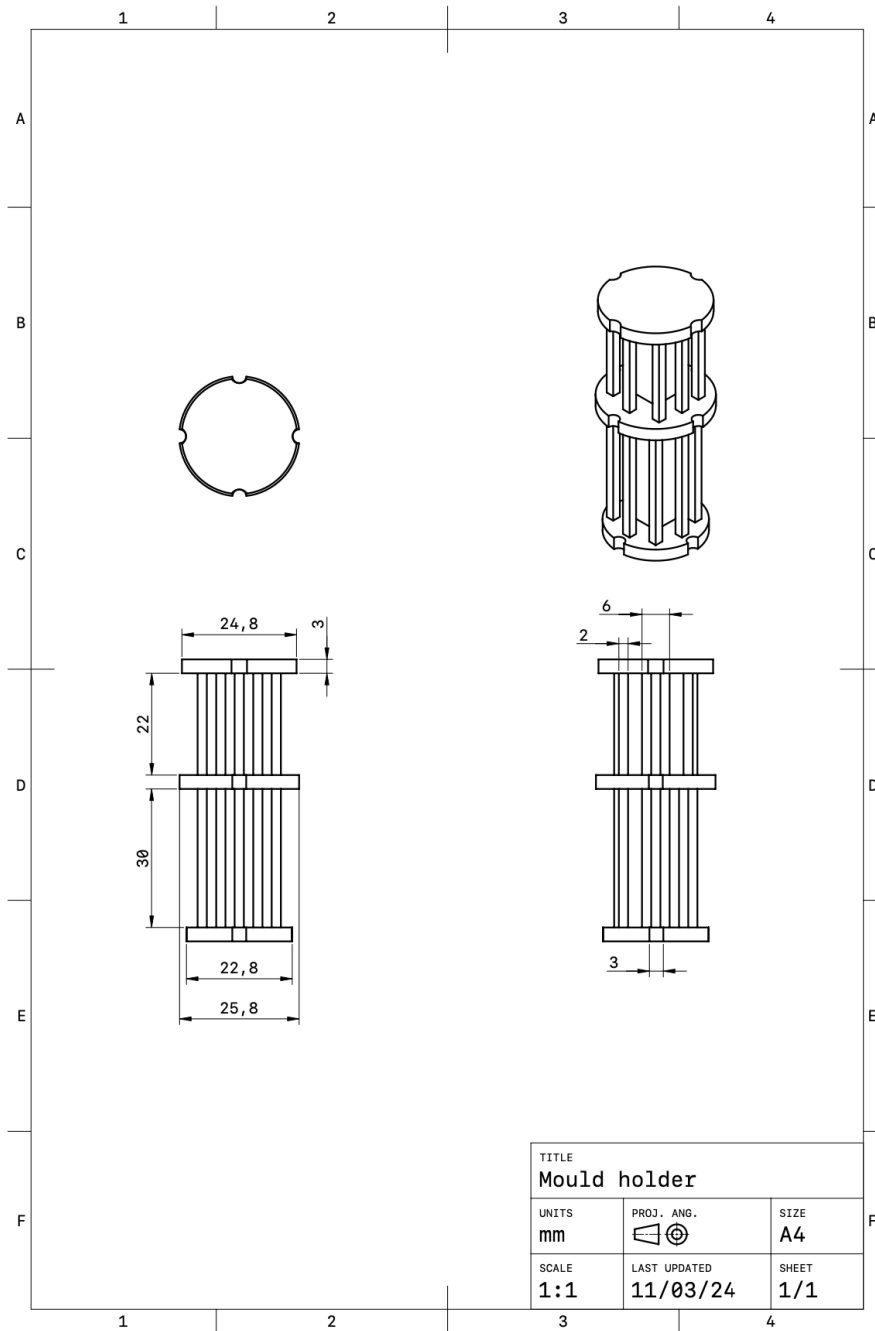


Fig. 26: Technical drawing of the holder designed for a 50 mL falcon tube for stabilization during centrifugation.

## 2. Agarose mould ethanol sterilization

The normal fabrication procedure of producing sterile agarose moulds is explained in method section 1. However, producing the agarose moulds in a non-sterile way and placing them in ethanol over night was tested to simplify the fabrication process. The outcome can be seen in Fig. 27 and shows a tissue area reduction of 16.61% after 48 hours. Comparing this to the experiment in results section 4.2 where the same spheroid batch was used, it can be observed that the tissue compaction is slower when using agarose moulds sterilized with ethanol (normal mould fabrication: tissue reduction of 24.09% after 48 hours). This indicates that this process has to be optimized for example by increasing the equilibration time to remove all ethanol from the moulds.

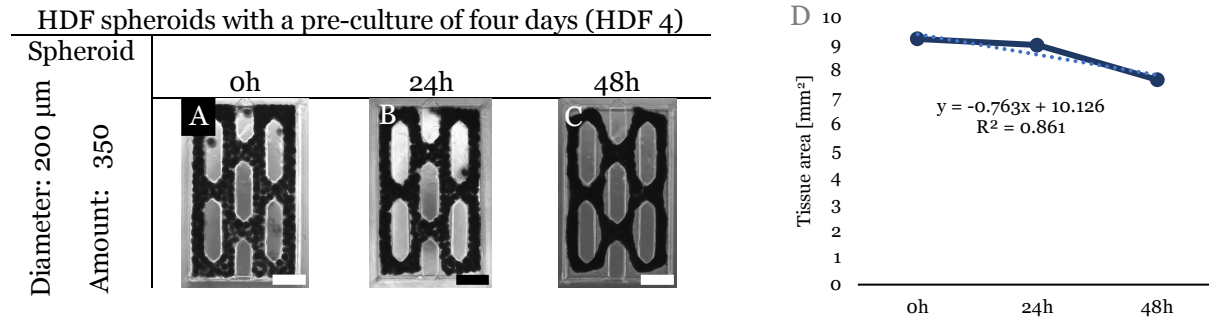


Fig. 27: HDF spheroid fusion of pre-culture day four seeded in moulds sterilized with ethanol (A to C) at time point 0, 24 and 48 hours and the tissue area analysis over time (0, 24, 48 hours) (D). One technical replicate from one independent experiment.



### 3. Human cardiomyocytes spheroid fusion

#### Method:

The normal fabrication procedure of producing sterile agarose mould is explained in method section 1. Primary Human Cardiac Myocytes (HCM, C-12810) were cultured in Myocyte Growth Medium (C-22070) purchased from Promocell®. After a reaching a confluency of 80%, cells were detached, and spheroids were created using the Corning® Elplasia® 12K flask (see method section 2.2).

#### Results:

Fig. 28 presents primary human CM spheroids of a pre-culture time of three days (HCM 3) seeded into agarose mould with a pillar height of 1 mm. The tissue area reduction is 1.81% after 9 hours and a total area reduction after 120 hours was 24.54%. Comparing this to the experiment in results section 4.2 and 4.3, then it can be observed that HCM spheroid causes the slowest tissue area reduction out of the three tested cell types (HDF 3 and 4, CM-HDF and HCM). This is also visualized by the linear equation in Fig. 28 G.

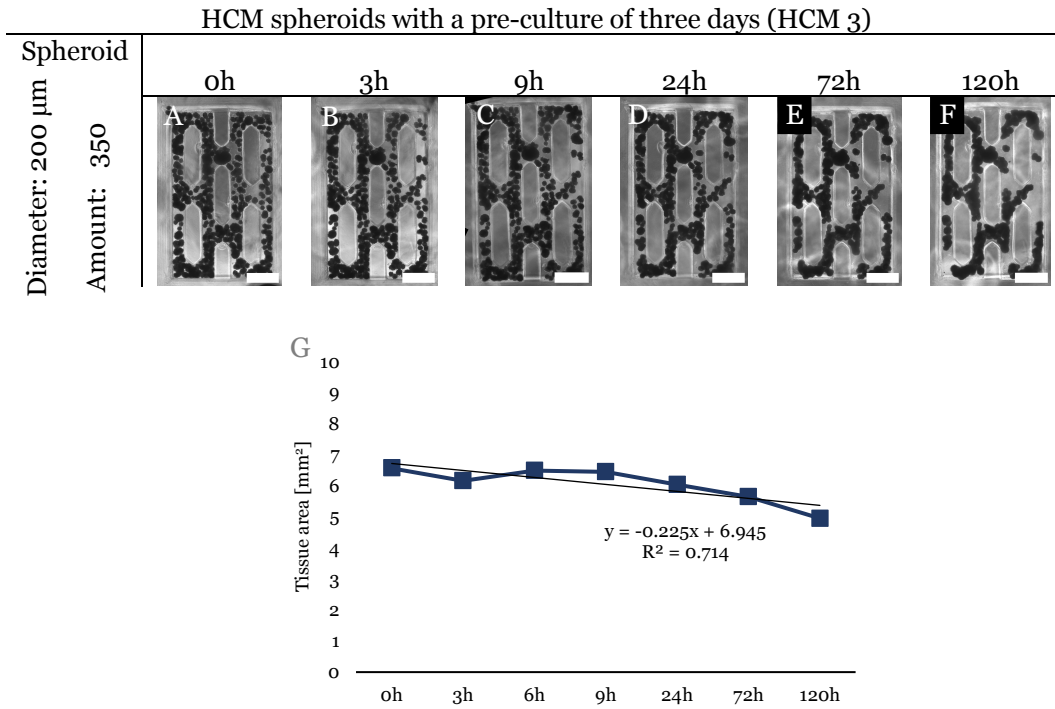


Fig. 28: HCM spheroid fusion analysis (G) of pre-culture day three seeded in moulds and imaged at 0, 3, 9, 24, 72 and 120 hours (A to F). One technical replicate from one independent experiment. Scale bar 1 mm.